Earth-Science Reviews 233 (2022) 104153

Contents lists available at ScienceDirect

Earth-Science Reviews

journal homepage: www.elsevier.com/locate/earscirev

Relative continent - mid-ocean ridge elevation: A reference case for isostasy in geodynamics

Thomas Theunissen [a,*], Ritske S. Huismans [a], Gang Lu [a], Nicolas Riel [b]

[a] Department of Earth Science, University of Bergen, Norway
[b] Johannes Gutenberg-Universitt, Institute for Geosciences, Mainz, Germany

ARTICLE INFO

Keywords:
Isostasy
Geodynamic modeling
Melt prediction
Mid-ocean ridge
Mantle
Depletion
Thermodynamic solution
Earth relief
Lithosphere

ABSTRACT

The choice of crustal and mantle densities in numerical geodynamic models is usually based on convention. The isostatic component of the topography is not calibrated to fit observations resulting in not very well constrained elevations. The density distribution on Earth is not easy to constrain because it involves multiple variables (temperature, pressure, composition, and deformation). We aim in this study to provide a reference case for geodynamic modelling where crustal and mantle densities are calibrated to fit the relative continent/mid-ocean ridge elevation in agreement with observations. We first review observed Earth topography of stable continents and of active mid-ocean ridges and define the characteristic average elevation of these domains. We use self-consistent thermodynamic calculations of dry mantle rocks that include partial melting to calibrate densities of the continental lithospheric mantle and beneath the mid-ocean ridge. The thermodynamic solutions are coupled with a 2-D incompressible plane strain finite element method for viscous-plastic creeping flows to solve for the dynamic evolution during extension from continental rifting to mid-ocean spreading. The combined results from 2-D thermo-mechanical models and 1-D isostatic calculations show that the relative elevation difference between mid-ocean ridges and continents depends on crustal density, mantle composition, and the degree of depletion of the lithospheric mantle. Based on these results we calibrate the reference density that only depends on temperature, which can be used in classic thermo-mechanical models based on the Boussinesq approximation. Finally the model calibration provides a solution that fits (1) the elevation of active mid-ocean ridges far from hotspots (-2750 ± 250 m), (2) the elevation of stable continents far from hotspots ($+400 \pm 400$ m), (3) the average depletion buoyancy of the continental lithospheric mantle (between -20 and -50 ± 15 kg/m^3 depending on lithospheric thickness) and (4) the average continental crust density (2835 ± 35 kg/m^3 for a 35 km thick crust).

1. Introduction

Isostasy is a fundamental element of Earth's lithosphere and topography evolution (e.g., Turcotte and Schubert, 1982; Watts, 2001; Molnar et al., 2015; Gvirtzman et al., 2016; Guerri et al., 2016; Davies et al., 2019; Lamb et al., 2020, and references therein) which is defined by the gravitational equilibrium of mass in the Earth's outer layers. At equilibrium, without other external forces, all regions of the Earth with identical elevation have the same buoyancy when referenced to the same compensation level, i.e. commonly at shallow upper-mantle depths. Together with crustal and mantle rheologies, local and regional isostasy control the topography of the Earth surface (Airy, 1855; Pratt, 1859; Heiskanen and Moritz, 1967; Forsyth, 1992; Watts, 2001). The ratio of crust versus mantle density controls the local or regional isostatic response to crustal thinning, thickening, erosion and deposition (Molnar and England, 1990; Bishop, 2007; Braun et al., 2013; Wolf et al., 2022; Watts and Ryan, 1976; McKenzie, 1978; Roberts et al., 1998; Crosby et al., 2011). Simple crustal Airy isostasy has been used to analyse compensation of continental topography assuming zero strength of the lithosphere and a negligible density contrast between mantle lithosphere and sub-litospheric mantle (e.g., Lamb et al., 2020; Watts, 2021). Power-spectral analysis of topography reveals that loading-related flexure considering the strength of the lithosphere explains the short- and medium wavelength signal ($100 < \lambda < 1000$ km) (e.g., Watts and Moore, 2017; Watts, 2021). At shorter wavelength, fault-related topography is isostatically uncompensated. Longer wavelength

* Corresponding author.
E-mail address: thomas.theunissen@uib.no (T. Theunissen).

https://doi.org/10.1016/j.earscirev.2022.104153
Received 12 January 2022; Received in revised form 14 July 2022; Accepted 6 August 2022
Available online 18 August 2022

topography ($1000 < \lambda < 3000$ km) can be explained by Airy isostasy while wavelength longer than 3000 km is thought to be caused by lithospheric thinning or thickening, or by deeper density anomaly embedded in the convective mantle, or by the dynamic effects of mantle flow (i.e., dynamic topography). Putting constraints on dynamic topography requires good understanding of the degree of isostatic compensation which directly depends on the density structure of the crust, mantle lithosphere, and sub-lithospheric mantle (Braun, 2010; Guerri et al., 2016; Hoggard et al., 2017; Davies et al., 2019; Flament, 2019). Knowledge about the density and thicknesses of the crust and mantle is consequently critical to understand and predict variations of Earth topography.

Geodynamic models allow self consistent study of crust and lithosphere deformation (Burov and Poliakov, 2003; Huismans and Beaumont, 2003; Lavier and Manatschal, 2006; Huismans and Beaumont, 2008; Huismans and Beaumont, 2011; Brune et al., 2014; Svartman Dias et al., 2015; Duretz et al., 2016). More and more geodynamic models also include the effect of erosion and sedimentation to understand the feedback between tectonic and surface processes (Theunissen and Huismans, 2019; Andrés-Martínez et al., 2019; Duretz et al., 2020; Allen and Beaumont, 2016; Goteti et al., 2012). However, geodynamic models are often not very well calibrated to observed topography. These studies typically use average reference values for crust, continental mantle lithosphere, and sub-lithospheric mantle densities from gravity modeling, seismology, and laboratory experiments that are not calibrated to variations of Earth topography. As a result, the accommodation space for sediments and the local or regional isostatic response to loading and unloading are usually not very well assessed. This is particularly obvious during formation of rifted passive margins where accommodation space for sediments is generally over-estimated (Svartman Dias et al., 2015). The general practice in modelling earth density structure and topography is to choose the reference column at a mid-ocean ridge (MOR), where the average density and elevation can be estimated with relatively good accuracy (e.g., Lachenbruch and Morgan, 1990; Afonso et al., 2008; Afonso et al., 2019). This practice also inherits from the historical assumption that a steady-state mid-ocean spreading center is in isostatic balance with a stable continental lithosphere (e.g., Coblentz et al., 1994, and references therein). However using standard reference densities results in a poor prediction of the relative elevation of stable continents and mid-ocean ridges (MOR).

Petrological and geochemical studies of basalts and basaltic rocks provide the base of the knowledge about the thermal structure and composition of the mantle (e.g., Niu, 2017; Niu, 2021). Based on chemistry of mid-ocean ridge basalts, the sub-lithospheric upper-mantle far from hotspots and far from subduction zones can be seen as statistically homogeneous both in terms of temperature and composition (e.g., Zindler and Hart, 1986; Meibom and Anderson, 2004; Anderson, 2007). The shear wave velocity structure of the upper-mantle beneath oceans shows a relatively homogeneous sub-lithospheric mantle beneath mid-ocean ridges (200–600 km depth) with slightly slower S-waves beneath the Pacific compared to other oceanic domains, and a clear signature of thermal necking and melting processes at mid-ocean spreading centers (30–110 km depth) (e.g., Schaeffer and Lebedev, 2013; French and Romanowicz, 2014; Celli et al., 2020). However, compositional variations of basalts also correlate with axial ridge depth because the extent of melting in the mantle, which mostly depends on spreading rate, also depends on degree of fertility of the source implying compositional variations in the mantle (Niu, 2017). The inferred compositional variations in the mantle imply that the reference mantle potential temperature (intersection of the adiabatic geotherm with the surface) beneath mid-ocean ridges far from hotspots is relatively homogeneous ±50 K (Niu, 2017). These chemical heterogeneities are caused by mantle convection and continuous mixing of deep lower-mantle, delaminated lithospheric mantle, and recycled subducted oceanic lithosphere (e.g., Stixrude and Lithgow-Bertelloni, 2012; Liu et al., 2008; Yan et al., 2020; Liu et al., 2022). However, bulk density variations in the sub-lithospheric mantle resulting from these compositional variations are suggested to be small, in the range 3–7 kg/m^3 (Fullea et al., 2021). Melt volume produced at mid-ocean ridges far from hotspots is a consequence of passive upwelling of mantle rocks and decompression melting that results in a global average oceanic crustal thickness of 6 km with variations between 4 and 8 km (e.g., Christeson et al., 2019; White et al., 2001). Parametric and petrological models explain the first order melting processes beneath mid-ocean ridges and can be used to predict oceanic crust thickness (e.g., McKenzie and Bickle, 1988; Niu and Batiza, 1991; Kinzler and Grove, 1992; Scott, 1992; Katz et al., 2003; Langmuir and Forsyth, 2007; Asimow et al., 2001; Behn and Grove, 2015; Jennings and Holland, 2015; Crameri et al., 2019; Simon et al., 2009; Lu and Huismans, 2021). Geodynamic modelling coupled with melt prediction can be used to constrain a reference mid-ocean ridge column that allows isostatic calculations and calibration of crustal and mantle densities assuming a statistically homogeneous sub-lithospheric upper-mantle far from hotspots and subduction zones characterised by a bulk fertile peridotite composition and a reference mantle potential temperature.

The first test, any density distribution of the continental and oceanic lithosphere and sub-lithospheric mantle should pass, is that it accurately predicts the elevation difference between stable continental topography and the elevation of mid-ocean ridges. Here we first provide a global analysis of Earth surface topography to constrain the average elevation of continents and mid-ocean ridges and their variability. We then present the methodology and results from thermodynamic calculations that are used to compute the density distribution with depth in the mantle for various compositions and to constrain the average depletion buoyancy of continental lithospheric mantle (CLM). We then present a 2-D thermo-mechanical model coupled with melt prediction and a self-consistent thermodynamic solution for the density distribution in the lithospheric and sub-lithospheric mantle to solve for visco-plastic flow and thermal structure during extension from rifting to steady state mid-ocean spreading center to predict the relative elevation between stable continents and mid-ocean ridges and the density structure beneath the mid-ocean ridge. The 2-D thermo-mechanical simulations include mantle melting and are used to calibrate the depletion buoyancy of the CLM, continental crustal density, and reference mantle density based on 1-D isostatic calculations (Fig. 1). Finally results from the 2-D thermo-mechanical models and from the 1-D isostatic calibration are presented and discussed. This study provides a reference case where crustal and mantle densities are calibrated to fit mid-ocean ridge elevation relative to the average elevation of stable continental lithosphere consistent with geophysical observations and thermodynamic calculations.

2. Global analysis of Earth topography

2.1. Data

We use the ETOPO-1 dataset to analyze variations of Earth topography (Amante and Eakins, 2009). The digital elevation model ETOPO-1 is smoothed using a median geospatial filter with a radius of 50 km to remove high frequency relief variations that are a consequence of local flexural effects (e.g., fault activity) or local magmatic relief (e.g., seamounts). For the continental domain only, elevations are corrected from ice and sea water load when required assuming local isostasy ($\rho_{i/w} h_{i/w} / \rho_m$ where $\rho_{i/w}$ is the density of the ice or the sea water, respectively 917 and 1030 kg/m^3 and ρ_m the density of the mantle, 3400 kg/m^3 corresponding to the density of the mantle close to the lithosphere-asthenosphere boundary that defines the compensation depth). All data used in this analysis are resampled into the same regular 2 arc-minutes resolution grid (Figs. S1 and S2).

We define two domains: (1) active mid-ocean ridges and (2) stable continental areas. Areas located closer than 1000 km from hotspots are excluded in order to remove the effect of mantle anomalies on the

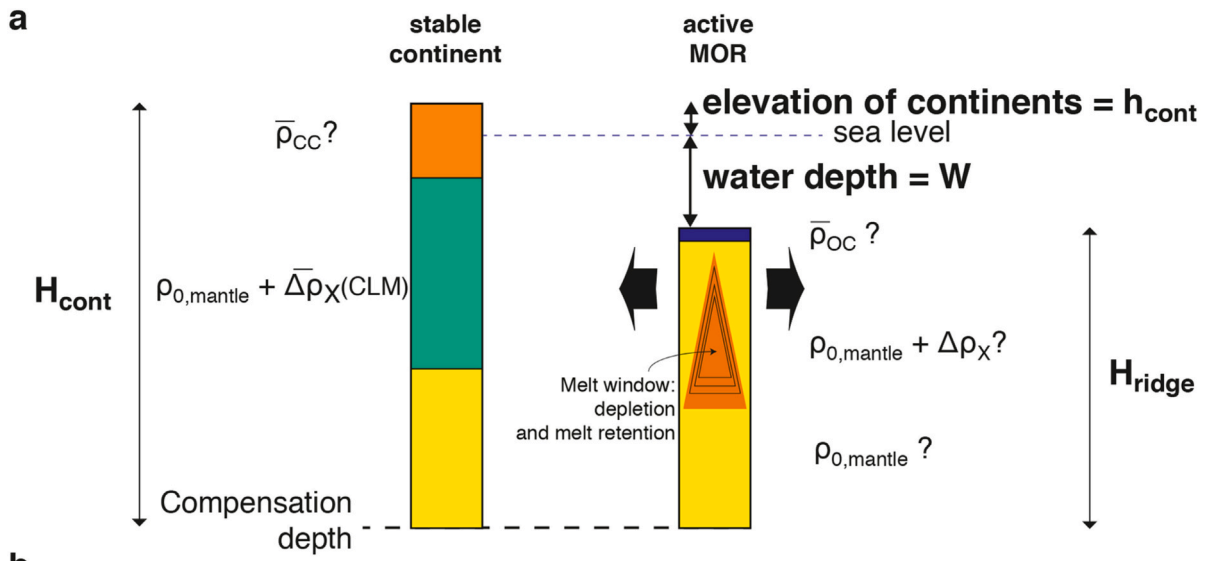

b

Process	Observables	Variables	Calibration by fitting
Melt production	• Oceanic crust, MORB (geophysics, ophiolites, samples, geochemistry)	• potential mantle temperature • upward mantle flux, spreading rate • mantle composition (solidus, liquidus, latent heat) (assuming negligible melt trapping and retention)	Oceanic crust thickness using melt prediction models
Mantle depletion, phase changes	• Xenolliths, outcrops (geochemistry, laboratory experiments) • Density profiles from geophysics	• mantle composition (considering only the upper-mantle < 300 km)	Density profiles from geophysics using thermodynamic calculations
Isostasy	• Elevation of continents and mid-ocean ridges.	• Average density of the: • continental crust • oceanic crust • sub-continental lithospheric mantle • mantle in the melt window	(1) continental crust density. (2) depletion buoyancy of the CLM. (3) elevations of the continents and of the MOR. using 2-D coupled melting thermo-mechanical modelling

Fig. 1. Principle developed in this study: calibration of the density structure to fit the relative elevation between continent and mid-ocean ridge. **a**, Schematic representation of the two reference columns including symbols used for average continental and oceanic crustal densities and density reduction due to melt extraction (depletion buoyancy) of mantle rocks calibrated in this study. Orange: continental crust; Blue: Oceanic crust; Green: Lithospheric continental mantle; Yellow: sub-lithospheric mantle. **b**, Description of the calibration procedure. The relative elevation between continent and mid-ocean ridge is estimated based on observations (Section 2). Thermodynamic solutions of characteristics bulk compositions of the upper-mantle provide constraints on average depletion buoyancy of the continental lithospheric mantle (CLM) (Section 3). Thermo-mechanical model coupled to thermodynamic solution (Section 4) allows for the 1-D calibration of the relative MOR-continental elevation by fitting average depletion buoyancy of the CLM and of the average continental crust density. Finally, the reference mantle density used in classical incompressible 2-D thermo-mechanical with Boussinesq approximation can then be calibrated based on this result (Fig. 10).

elevation of the Earth surface (Fig. S2a). We use the hotspot database (72 hotspots) from Morgan and Morgan (2007) without consideration about their origin (Courtillot et al., 2003). To characterize mid-ocean ridges we use grids of seafloor ages and spreading rates from Müller et al. (2008). The axis of active mid-ocean ridges with a point every 25 km is constructed using seafloor ages lower than 0.5 Ma (Fig. S3). The maximum elevation in a radius of 75 km of each point defines the MOR elevation while the median of the spreading rate in the same radius provides the spreading rate. We ignore sedimentation at the ridge as pelagic sediment thickness is on average lower than 200 m (e.g., Straume et al., 2019).

To characterize the stable continental areas we use grids of the horizontal strain rate from Kreemer et al. (2014), continental crustal thickness from the gravity model of Reguzzoni and Sampietro (2015), lithospheric thickness from Steinberger and Becker (2018) and age of the continental lithosphere by Poupinet and Shapiro (2009). All points with a strain rate lower than 10^{-16} s^{-1} and a crustal thickness of 35 ± 5 km are used to define stable continental areas (Figs. 2 and S6). The lithospheric thickness and age of the continental lithosphere are used to assess the sensitivity of continental elevation to these parameters.

2.2. Analysis of active MOR and stable continental elevation

The distribution of active MOR elevation far from hotspots is unimodal with an average of about -2750 ± 250 m (Fig. 2). We note that this value is close to the estimate of the zero-age ridge elevation (e.g., Richards et al., 2018) and close to the modal depth of the bathymetry analysis of Rowley (2018). The MOR elevation is sensitive to full

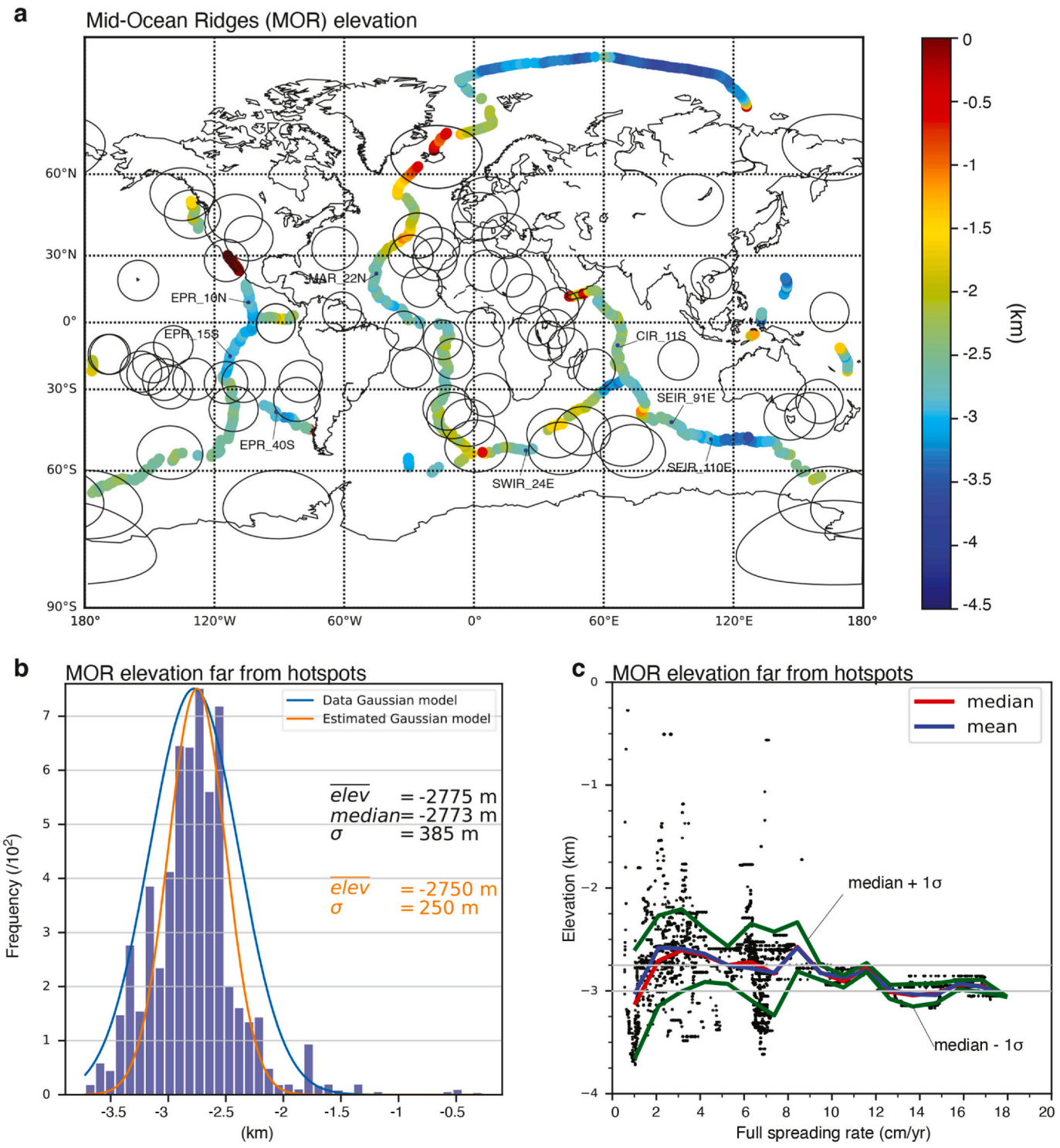

Fig. 2. Mid-ocean ridge elevation based on filtered ETOPO-1 grid. **a**, Points selected on the grid following the procedure described in Fig. S3. Circles with a diameter of 2000 km represent hotspots from Morgan and Morgan (2007). **b**, Statistics of MOR elevation far from hotspots. **c**, sensitivity of the MOR elevation far from hotspots to the spreading rate. Statistics of MOR elevation close to hotspots and the distribution of the present day spreading rate can be found in supplemental Fig. S4.

spreading rate. For values between 2 and 9 cm/yr, the elevation of MOR is rather constant and exhibits an average elevation of about −2700 m. Ultra-slow spreading ridges are deeper up to about −3600 m for full spreading rate lower than 1 cm/yr. Very fast spreading ridges above 9 cm/yr exhibit an average depth of about −3000 m. Most spreading ridges have a full spreading rate lower than 9 cm/yr. MOR elevation close to hotspots is about 250 m shallower on average (Fig. S4). Comparisons between high-resolution bathymetric profiles through various MOR and our results show that the smoothing procedure adopted here is satisfying (Fig. 3).

The elevation of continents exhibits a high variability (Figs. 4 and 5). The elevation of stable continents far from hotspots with a crustal thickness between 30 and 40 km has a mean of about +420 ± 390 m and a median of +440 m with a right skewed distribution (Fig. 4b). The median is representative of the characteristic elevation of stable continents. We note that the selected area of Antarctica exhibits higher

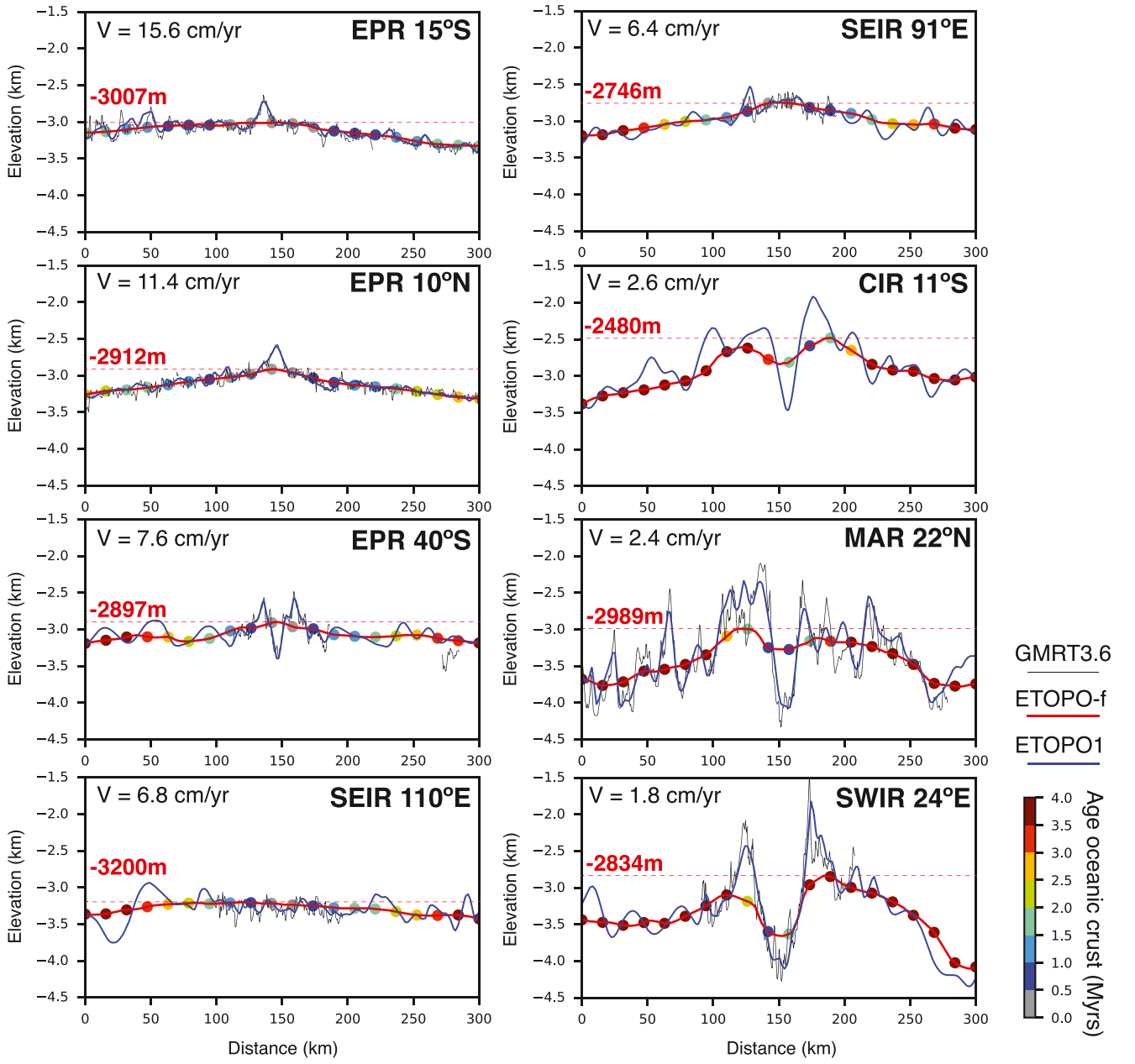

Fig. 3. Bathymetric profiles across mid-Atlantic (MAR), East-Pacific (EPR), Southwest Indian (SWIR) and Southeast Indian (SEIR) oceanic ridges. High-resolution bathymetric profiles are from the GMRT 3.6 dataset (Ryan et al., 2009). The filtered bathymetric profile (ETOPO-f) is from this study. Spreading rates are from Müller et al. (2008). Location of these profiles can be found in Fig. 2.

elevation +800 m on average in part responsible for this distribution (Fig. S5). Close to hotspots, continents are higher in the range 100–300 m with an average of about $+530 \pm 390$ m (Fig. 4c). The main factor controlling the elevation of stable continents is the crustal thickness (Fig. 5b). On average, the crustal thickness of stable continents far from hotspots is 35 ± 5 km and exhibits a left skewed distribution (Fig. 5c). The mean elevation of the continents is about $+400 \pm 400$ m for a crustal thickness of 35 km (Fig. 5b). The elevation of stable continents depends to a lesser extent on lithospheric thickness and lithospheric age. Areas with thin lithosphere exhibit higher elevations up to +600 m while it is about +200 m with 250 km thick lithosphere but the correlation between elevation and lithospheric thickness is relatively weak (Fig. 5d). Proterozoic continental lithosphere exhibits higher elevations up to +500 m while lithospheres with different age have an elevation of about +250 m (Fig. 5e). We use $+400 \pm 400$ m as a characteristic average elevation for stable continents with a crustal thickness of 35 ± 5 km. The relative elevation between continents and MOR is consequently about 3150 m with a characteristic water depth at the ridge of 2750 m.

3. Thermodynamic calculations of mantle density

Density changes in the mantle are the consequence of variations of solid state phase changes, melting, and the intrinsic P-T-dependence for a given phase composition. Thermodynamic calculations of phase equilibria for given bulk-rock composition provide a mapping of physical properties as a function of pressure and temperature. We use recent advances in thermodynamic calculations of dry mantle rocks that include partial melting to compute the density as a function of pressure and temperature and to estimate the density reduction by depletion (depletion buoyancy) owing to partial melting. These calculations

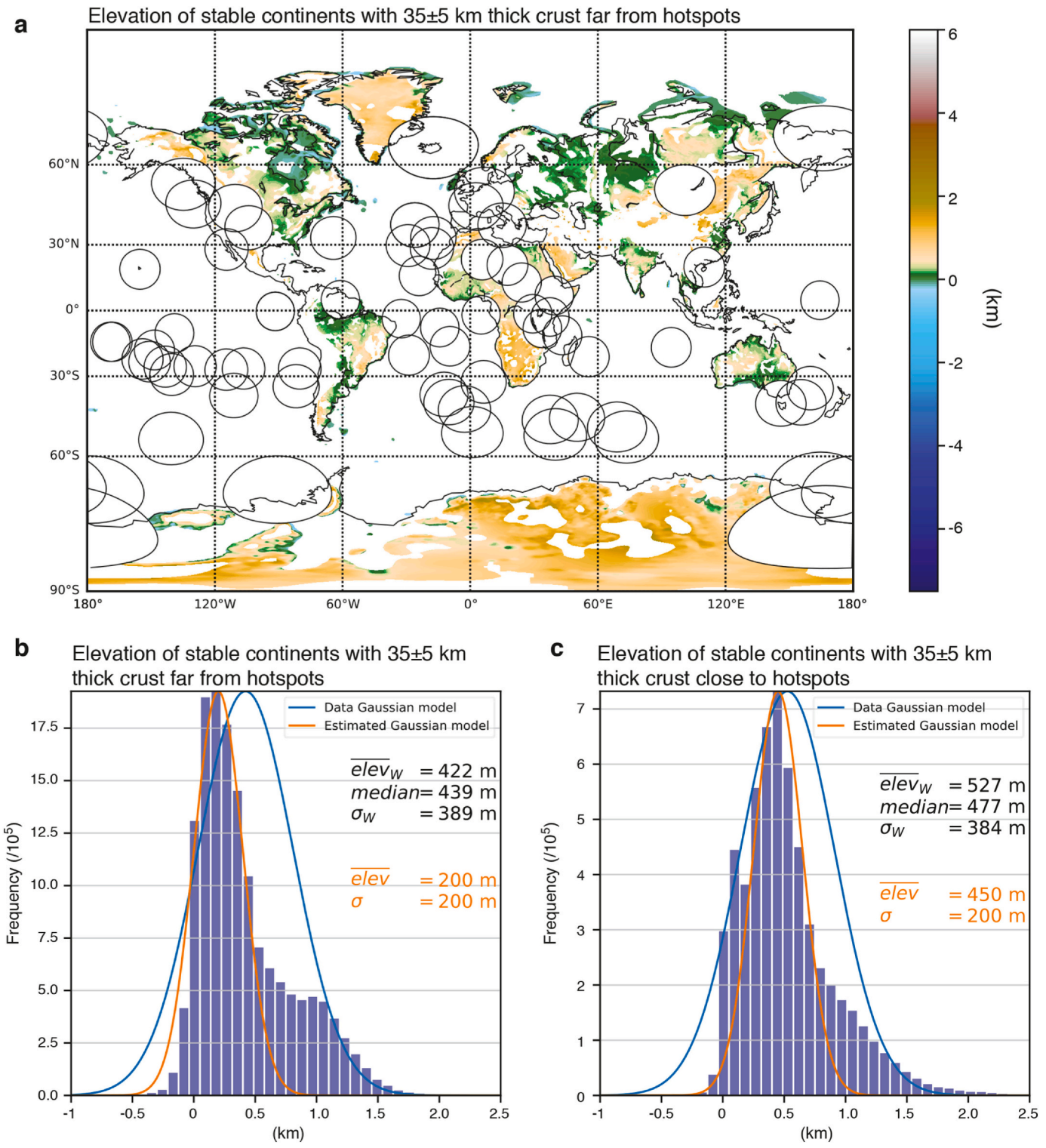

Fig. 4. Stable continental elevation based on filtered ETOPO-1 grid. **a**, Points selected on the grid where topography is higher than 0 m, $\dot{\varepsilon_H} < 10^{-16}$ s^{-1} (Kreemer et al., 2014), crustal thickness is between 30 and 40 km (Reguzzoni and Sampietro, 2015) and located further than 1000 km from hotspots. Circles with a diameter of 2000 km represents hotspots from Morgan and Morgan (2007). **b**, Statistics of stable continental elevation far from hotspots. **c**, Statistics of stable continental elevation close to hotspots.

provide a way to constrain the density structure of the mantle beneath continents and mid-ocean ridges.

In order to generate the phase equilbria in the mantle (including suprasolidus conditions) we used the thermodynamic dataset from Jennings and Holland (2015). Phase diagrams were produced using Perple_X 6.8.4 and the hp622.dat thermodynamic database for pure species and end-members (Holland and Powell, 2011). We used the following set of solution phases: O(JH), Sp(JH), Pl(JH), Melt(JH), Grt (JH), Opx(JH), Cpx(JH), Eskol(C), Ring(H), for olivine, spinel, plagioclase, melt, garnet, orthopyroxene, clinopyroxene, eskolaite and ringwoodite, respectively (Jennings and Holland, 2015; Holland et al., 2013; Chatterjee et al., 1982). Considering Cr and eskolaite (Cr_2O_3) in the

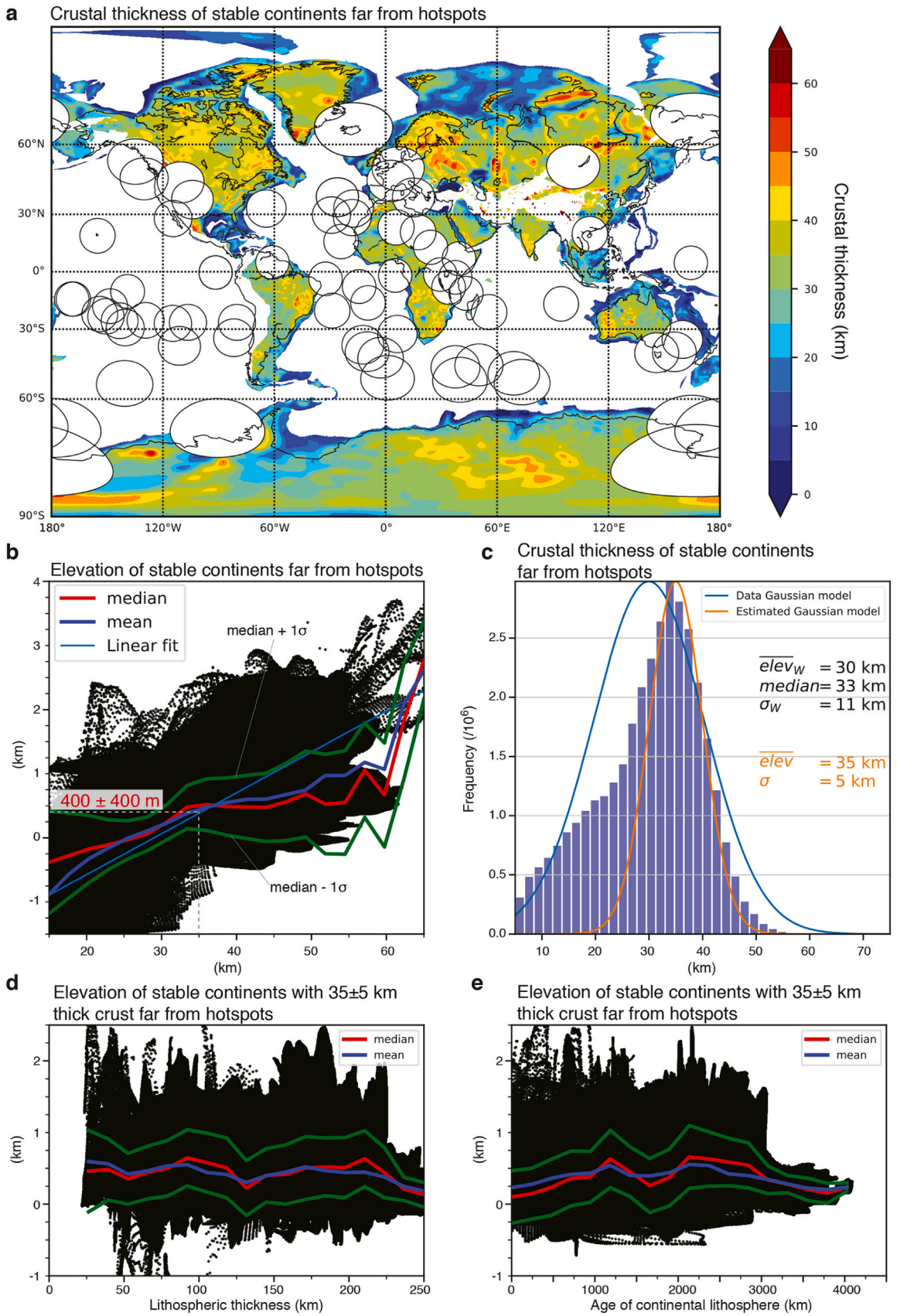

Fig. 5. Continental crust thickness and stable continental elevation variability with respect to crustal thickness, lithospheric thickness and lithospheric age. **a**, maps of continental thickness far from hotspots and $\dot{\varepsilon_H} < 10^{-16}$ s^{-1} (Kreemer et al., 2014). **b**, Variability of the continental elevation to crustal thickness from Reguzzoni and Sampietro (2015). **c**, Variability of the continental elevation to lithospheric thickness from Steinberger and Becker (2018). **d**, Variability of the continental elevation to lithospheric age from Poupinet and Shapiro (2009).

Table 1
Characteristic bulk compositions in the 7 components NCFMASCr (ferric iron free) system used in this study.

Sub-lithospheric mantle fertile compositions				
	MS	**J79**	**SP2008**	**KLB-1**
SiO_2	45.12	45.39	45.54	44.95
Al_2O_3	4.51	4.02	4.53	3.52
Cr_2O_3	0.38	0.46	0.41	0.32
FeO^T	8.12	7.83	8.18	8.22
MgO	37.90	38.46	37.78	39.62
CaO	3.61	3.51	3.10	3.08
Na_2O	0.36	0.33	0.45	0.30
Total	100.00	100.00	100.00	100.00
Mg#	89.27	89.75	89.17	89.57
Cr#	5.36	7.16	5.76	5.76

Continental lithospheric depleted compositions										
	SP2008_89low	**KC2004_93high**	**KC2004_93low**	**YLM2**	**YLM3**	**PLM1**	**PLM2**	**ALM1**	**ALM2**	**ALM0**
SiO_2	47.65	42.55	44.49	44.71	44.68	44.89	44.95	45.92	44.69	43.12
Al_2O_3	0.53	4.46	0.52	3.52	2.62	2.11	1.91	0.99	1.76	0.30
Cr_2O_3	0.43	0.41	0.42	0.40	0.40	0.42	0.40	0.28	0.30	0.40
FeO^T	8.56	6.09	6.36	8.04	8.25	7.93	7.96	6.43	8.15	6.53
MgO	39.53	43.28	45.25	39.98	41.36	42.58	42.93	45.71	43.69	49.45
CaO	3.25	2.78	2.90	3.11	2.52	1.91	1.71	0.59	1.28	0.10
Na_2O	0.05	0.45	0.05	0.24	0.18	0.15	0.12	0.07	0.12	0.10
Total	100.00	100.00	100.00	100.00	100.00	100.00	100.00	100.00	100.00	100.00
Mg#	89.17	92.68	92.69	89.87	89.93	90.54	90.58	92.69	90.52	93.10
Cr#	35.04	5.76	34.94	7.12	9.36	11.83	12.38	15.95	10.31	47.21

Concentrations are given in weight amount % oxide and normalized to total 100%. MS (McDonough and Sun, 1995). JS79 (Jagoutz et al., 1979). KLB-1 (Jennings and Holland, 2015; Takahashi et al., 1993; Davis et al., 2009). SP2008 (Simon and Podladchikov, 2008), KC2004 using sample 38-4(Kopylova and Caro, 2004), "low" and "high" refer to both sodium and aluminium concentration, 89 and 93 refer to the Mg#. FeO^T: total iron. Continental lithospheric mantle compositions are from Griffin et al. (1999); Griffin et al., 2008; Afonso et al., 2008. YLM: Young lithospheric mantle; PLM: Proterozoic lithospheric mantle; ALM: Archean mantle lithosphere. Equivalence with previous publications: YLM2 = Archon3, Average Tecton Gnt.; YLM3 = Average Tecton peridotite; PLM1 = Average Proton Gnt.; PLM2 = Prefered Proton; ALM1 = Archon 0, Average Archon Gnt.; ALM2 = Archon 2, Average Archon Kaapvaal High-T Lherzolite; ALM0 = Archon 1, Estimate Archon "Pristine".

thermodynamic calculations allows constraining transitions of Al-bearing phases (plagioclase-spinel-garnet) which are responsible for strong density variations (Klemme, 2004; Klemme et al., 2009; Jennings and Holland, 2015; Ziberna and Klemme, 2016). The melt phase and corresponding melt fraction is self-consistently predicted along with the other solid solution phases providing the most stable mineral (and melt) assemblage. This implies that solidus, melt fraction, and phase assemblage are computed as function of the bulk-rock composition and P-T conditions.

Computations were made between 200 °C and 1650 °C and between 0 and 6 GPa, which corresponds to about 170 km depth. Such a pressure–temperature range covers all critical phase changes at shallow upper-mantle depths including low pressure phase reactions such as garnet-spinel-plagioclase, and partial melting. Outside the calibration range, physical properties are extrapolated below 200 °C and between 6 GPa and 21 GPa. Here we ignore the phase transition at 410 km which has little significance for rifting and MOR spreading geodynamics.

We modelled for benchmark purposes the phase diagram of the reference KLB-1 fertile dry mantle composition (e.g., Davis et al., 2009) using the last thermodynamic database, which shows that the overall pattern of the topology of mantle phases below solidus and suprasolidus conditions is nearly identical with the published phase diagram from Jennings and Holland (2015). The slight differences are mainly due to the modelling approach of minimizing the Gibbs free energy of the assemblage (Fig. S7). The calculations also reproduce well the experimentally determined composition of the mineral assemblage and of the melts, which is critical when computing the density of the mantle (Jennings and Holland, 2015).

The reference bulk composition of fertile sub-lithospheric mantle and the continental depleted mantle lithosphere is not well constrained as the mantle composition is heterogeneous at all scales and is often the result of a complex history of melting, refertilization, and metasomatism. Sampling of mantle rocks is either related to mantle exhumation at passive margins or magmatic sampling that transport mantle xenoliths to the surface and is then potentially not representative of the bulk composition. Previous studies provided bulk compositions of the fertile sub-lithospheric mantle (Jagoutz et al., 1979; McDonough and Sun, 1995; Takahashi et al., 1993), and of depleted mantle lithosphere of varying age (Archean, Proterozoic, and Phanerozoic) based on xenolith data (e.g., Griffin et al., 1999; Griffin et al., 2008). Simon and Podladchikov (2008) using the end-member bulk composition of fertile and highly depleted (Archean) mantle created systematic intermediate compositions by mixing end-member bulk proportions of Al_2O_3 and Na_2O. Here we gather a set of 14 bulk compositions including 4 fertile and 10 depleted mantle (Table 1). Since the ratio of ferric iron content is not well constrained or not defined in the different bulk composition, we use a 7 component NCFMASCr system.

For each bulk composition we compute the thermodynamic solution and extract densities, thermal expansion, compressibility, and melt fraction (Figs. 6 and S8). We also compute for each bulk composition the density as a function of depth for a typical geotherm of a 125 km thick continental lithosphere with 35 km thick crust ($H = 0.9$ mW/m^3, $T_P =$ 1280°C and adiabatic gradient of 0.4 K/km, e.g., Table 3). The resulting density profiles are compared with density profiles constrained by geophysical observations (Fig. 7) (Dziewonski and Anderson, 1981; Kustowski et al., 2008; Ito and Simons, 2011). We select the bulk fertile composition that best matches the density structure of the sub-lithospheric upper-mantle as constrained by seismological and geodetic data (Dziewonski and Anderson, 1981; Kustowski et al., 2008; Ito and Simons, 2011). We assume that the bulk composition that provides a density profile similar to global 1-D profiles at depths below the average continental lithosphere-asthenosphere boundary is characteristic of the whole sub-lithospheric upper mantle. The fertile bulk composition SP2008 (Mg# = 89, high Al_2O_3, high Na_2O, see Table 1) from Simon and Podladchikov (2008) provides a good fit (Fig. 7a). This reference fertile mantle composition is used to compute the degree of

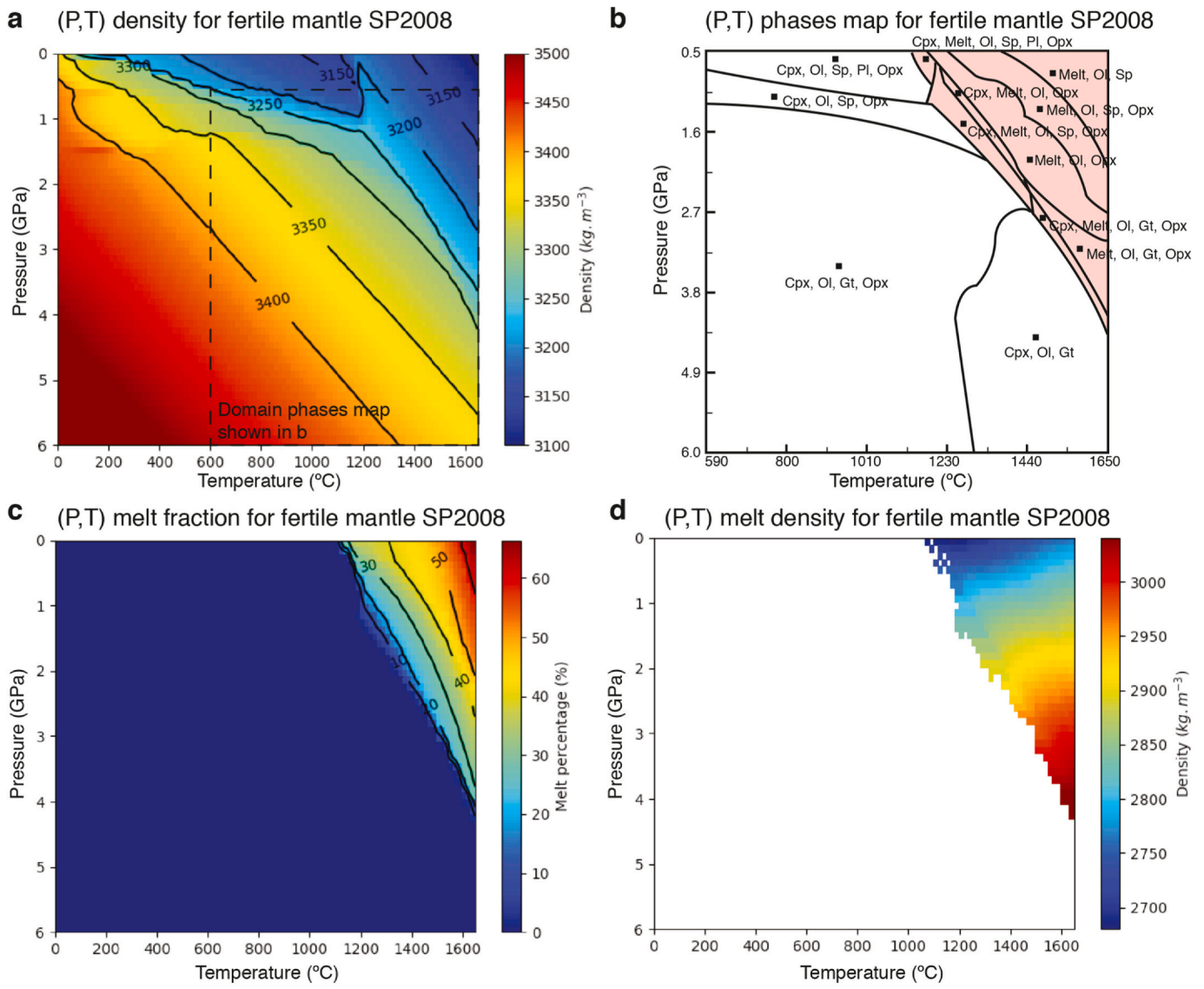

Fig. 6. Outputs from Perplex for a fertile composition (SP2008: #Mg = 89, high Al_2O_3, high Na_2O, see Table 1). **a**, Density of the solid phase, residual from melting inside the melt window. **b**, Phases map. **c**, Melt fraction. **d**, Melt density. Thermal expansion and compressibility of the residual are provided in supplemental Fig. S8.

depletion of other mantle rocks but also to compute the melt volume during decompression melting at mid-ocean ridges.

Using this reference fertile mantle composition it is then possible to compute the depletion buoyancy of the continental lithospheric mantle (CLM) (Fig. 7 and Table 2). We compute the average depletion buoyancy following:

$$\Delta\rho_X = \frac{1}{H_{CLM}} \cdot \int_{CLM} \left(\rho(P,T)_0 - \rho(P,T)_{0,fertile} \right) dz \quad (1)$$

where $\Delta\rho_X$ is the density reduction by depletion owing to melting or depletion buoyancy, H_{CLM} the thickness the CLM, and $\rho(P,T)_0$ the density for each mineral assemblage for varying P-T conditions normalised to surface conditions using:

$$\rho(P,T)_0 = \frac{\rho(P,T)}{(1-\alpha(P,T)(T-T_0))\cdot(1+\beta(P,T)(P-P_0))} \quad (2)$$

where P is the pressure, T the temperature, $\rho(P,T)$ the density at P-T conditions, $\alpha(P,T)$ is the thermal expansion at P-T conditions (See supplemental Fig. S8a), T_0 the temperature at surface conditions, $\beta(P,T)$ the compressibility at P-T conditions (See supplemental Fig. S8b), and P_0 the pressure at surface conditions. The resulting average density difference becomes independent of conditions of pressure and temperature and only depends on differences in composition. However, we note that the difference in the calculated depletion buoyancy is small in the order of 2 –5 kg/m^3 when using in situ density values because the variations of thermal expansion and compressibility with P-T conditions are similar whatever the composition (Table 2, Fig. S8). Calculations are made with a 125 km thick lithosphere but we show that there are little differences (< 2 –3 kg/m^3) when calculating the average density difference in the sub-lithospheric mantle and in the continental lithospheric mantle with different lithospheric thicknesses (Table 2). Using the set of characteristic mantle compositions based on xenolith studies (Jagoutz et al., 1979; McDonough and Sun, 1995; Kopylova and Caro, 2004; Afonso et al., 2008; Griffin et al., 1999; Griffin et al., 2008) (Table 2), we obtain an approximation of the depletion buoyancy of the lithospheric mantle for a Phanerozoic lithosphere $\Delta\rho_X \sim 10$ –20 kg/m^3 (compositions YLM2 and YLM3), for a Proterozoic lithosphere $\Delta\rho_X \sim 30$ –35 kg/m^3 (compositions PLM1 and PLM2) while it is larger than 40 kg/m^3 for Archean lithosphere (compositions ALM1, ALM2, ALM3, SP2008_89_low, KC2004_93_low) (Fig. 7 and Table 2).

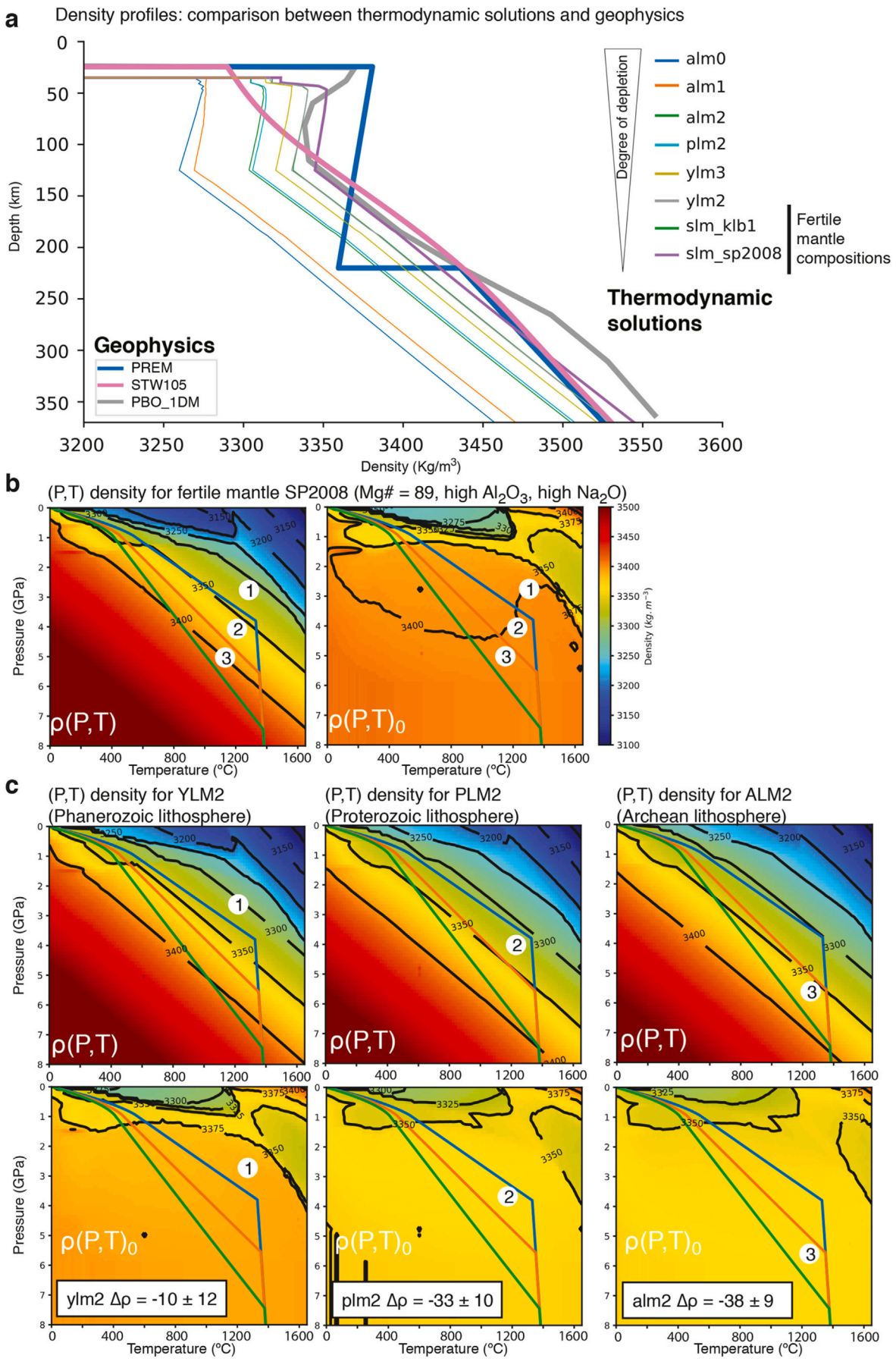

(caption on next page)

Fig. 7. Calibration of the depletion buoyancy of the mantle. **a**, selection of the most representative fertile mantle composition. Density profiles are calculated using thermodynamic solutions for bulk compositions presented in Table 1 along the geotherm of a 125 km thick Phanerozoic lithosphere with 35 km thick crust where $T_P = 1280°C$, adiabat is 0.4 K/km, Moho temperature is 550 °C. Those profiles are compared with three geophysical estimates of upper-mantle density: two global seismic models PREM (Dziewonski and Anderson, 1981) and STW105 (Kustowski et al., 2008) and one regional geodetic model from western United States PBO-1DM from Ito and Simons (2011). A figure including all bulk compositions can be found in supplementary material (Fig. S9). **b**, Left: Density map ($\rho(P,T)$) of the most representative fertile composition based on (a) (SP2008: Mg# = 89, high Al_2O_3, high Na_2O, see Table 1 and Fig. 6). Three geotherms corresponding to different lithospheric thicknesses are superimposed. Right: densities normalised to surface conditions ($\rho(P,T)_0$) (Eq. 2). Low pressure fields of spinel and plagioclase phases are visible. **c**, Depletion buoyancy of the CLM calculated using Eq. 1 for three bulk compositions characteristic of lithosphere with different age and thickness. Depletion buoyancy for Proterozoic or Archean characteristic bulk composition differ by less than 2 kg/m^3 with those calculated using the geotherm of the reference 125 km thick lithosphere (Table 2). On top density map and below densities normalised to surface conditions (Eq. 2). Depletion buoyancy for other representative bulk compositions of the CLM are provided in Table 2.

Table 2
Average densities normalised to surface conditions, $\overline{\rho}(P,T)_0$, and depletion buoyancy, $\Delta\rho_X$ (density reduction due to melt extraction), for the characteristic bulk compositions shown in Table 1.

Name	Calculated in the SLM		Calculated in the CLM	
	$\overline{\rho}(P,T)_0$	$\Delta\rho_X$	$\overline{\rho}(P,T)_0$	$\Delta\rho_X$
Characteristic SLM fertile bulk mantle composition				
SP2008	3403.7	0.0	3393.8	0.0
MS	3405.8	2.1	3396.3	2.5
JS79	3396.0	−7.7	3386.5	−7.3
KLB-1	3392.0	−11.5	3383.1	−10.7
Characteristic CLM depleted mantle composition				
YLM2	3392.5	−11.2	3383.5	−10.3
YLM3	3382.3	−21.4	3373.6	−20.2
KC2004_93high	3372.1	−31.6	3360.1	−33.7
PLM1	3369.6	−34.1	3360.9	−32.9
PLM2	3366.7	−37.0	3358.0	−35.8
ALM2	3364.8	−38.9	3356.3	−37.5
SP2008_89low	3356.8	−46.9	3348.0	−45.8
KC2004_93low	3334.4	−69.3	3326.0	−67.8
ALM1	3328.2	−75.5	3314.9	−74.4
ALM2	3328.1	−75.6	3319.6	−74.2

Results are given in kg/m^3. Bulk compositions are ordered according to their depletion buoyancy compared to SP2008. Computations are made along the geotherm of a 125 km thick lithosphere within the CLM or within the SLM using densities normalized to surface conditions, i.e. corrected from thermal expansion and compressibility (Eqs. 1 and 2). Standard deviation is about 10 kg/m^3. There is no big differences in the estimate of the depletion buoyancy, i.e. 2–5 kg/m^3, when computations are made along geotherms of thicker lithospheres or using density without correction from thermal expansion and compressibility (Figs. 7 and S8). KLB-1 (Jennings and Holland, 2015; Takahashi et al., 1993; Jennings et al., 2016). MS (McDonough and Sun, 1995). JS79 (Jagoutz et al., 1979). SP2008 (Simon and Podladchikov, 2008), KC2004 using sample 38-4 (Kopylova and Caro, 2004), "low" and "high" refer to both sodium and aluminium concentration.YLM: Young lithospheric mantle; PLM: Proterozoic lithospheric mantle; ALM: Archean mantle lithosphere (Griffin et al., 1999; Griffin et al., 2008; Afonso et al., 2008).

4. 2-D thermo-mechanical model

We use two different approaches in our geodynamic models to compute the density structure at the mid-ocean ridge. In the first, density is computed by using results of thermodynamic calculations that allows retrieving a realistic density structure. This realistic density structure then allows calibrating the continental crustal density and the average depletion buoyancy of the continental lithospheric mantle. In the second, the density is computed considering the effect of thermal expansion only applying the Boussinesq approximation as commonly done in geodynamic models. This second modelling approach allows calibrating the reference density of the sub-lithospheric mantle. We explain here the coupled thermo-mechanical modelling framework and the two different approaches to compute melt prediction and related depletion buoyancy in the mantle beneath the mid-ocean ridges during spreading.

4.1. Coupled thermo-mechanical framework

We use the 2-D finite-element geodynamic code FANTOM (Thieulot, 2011; Theunissen and Huismans, 2019) to model continental rifting to seafloor spreading. The code solves the Stokes and heat equations coupled through P-T dependent rheology and density Appendix A. The initial model geometry represents a 1,200 km wide and 600 km deep, idealized, crustal and upper mantle cross-section (Fig. S13, Table 3). It consists of a laterally uniform continental lithosphere with 35 km thick crust, 90 km thick lithospheric mantle, and sub-lithospheric upper mantle down to the lower model boundary. Continental rifting and mid-ocean spreading are modeled by applying extensional velocity boundary conditions of ±1.5 cm/yr in the lithosphere on both model sides (full spreading rate of 3.0 cm/yr). The upper surface is free and the side and bottom boundaries have free-slip boundary conditions. Outflow is balanced by a small distributed inflow on the side boundaries in the sub-lithospheric mantle domain. In order to ensure constant total mass, the average pressure along the bottom of the model is maintained constant by adjusting the influx of the sub-lithospheric mantle at the sides. This allows defining an absolute sea level within the model independent from surface displacement. Based on sea level, a water load is implemented in order to fully consider all mass loads on the free surface.

The initial temperature profile of the continent corresponds to 1-D thermal steady state and the underlying mantle has an adiabatic gradient of 0.4 K/km. The thermal setup reflects average values for Phanerozoic continental lithosphere (see Table 3), with a Moho temperature of 550 °C and 1330 °C at the base of the lithosphere, resulting in a surface heat flow of 51 mW/m^2 and mantle heat flux of 19.5 mW/m^2 (Hacker et al., 2015). We use constant thermal conductivity of $k = 2.25$ W/m/K in all materials, heat capacity equals 1270 J/K/kg in the mantle and 1050 J/K/kg in the continental and oceanic crust. The side boundaries are insulated and the bottom boundary has a fixed temperature boundary condition of 1520 °C. This setup results in mantle potential temperature of 1280 °C. In the thermal calculation the initial temperature is laterally uniform except at the LAB where a small thermal anomaly is included to promote lithospheric necking in the center.

We employ a strong crustal rheology which promotes the formation of narrow margins. Our model materials account for strain weakening by linearly reducing the effective angle of internal friction and cohesion as a function of accumulating plastic strain which allows strain localizastion (Buck, 1993; Huismans and Beaumont, 2002; Lavier et al., 1999; Lavier et al., 2000). The sub-lithospheric mantle is fully weakened inhibiting strain localization following exhumation to the seafloor which ensures a symmetric spreading and a smooth relief at the seafloor. We introduce a 400 km wide zone of statistical noise in the initial plastic strain in the frictional upper-crust and upper-mantle lithosphere that represents inherited weakness.

The reference density at $T = 0°C$ in the continental and oceanic crust are respectively set to 2835 kg/m^3 and 2900 kg/m^3 and vary with temperature using a constant thermal expansion of $3.0 \cdot 10^{-5}$ K^{-1} following:

Table 3
Thermal, melt production and rheological parameters.

Thermal parameters						
Mantle potential temperature	T_p	°C	1280			
Adiabatic gradient	$\frac{\delta T}{\delta z}$	$K{\cdot}km^{-1}$	0.4			
Thermal conductivity	k	$W{\cdot}m^{-1}{\cdot}K^{-1}$	2.25			
Crustal specific heat capacity	c_p	$J{\cdot}K^{-1}{\cdot}kg^{-1}$	1050			
Mantle specific heat capacity	c_p	$J{\cdot}K^{-1}{\cdot}kg^{-1}$	1270			
Continental crust heat production rate	H	$W{\cdot}m^{-3}$	$0.9{\cdot}10^{-6}$			
Crustal thermal expansion (and mantle in model M2)	α_T	K^{-1}	$3.0{\cdot}10^{-5}$			
Mantle thermal expansion (model M1)	$\alpha(P,T)$	K^{-1}	from thermodynamic calculations (Fig. S8)			
Mantle compressibility (model M1)	$\beta(P,T)$	Pa^{-1}				
Change in entropy on melting	ΔS	$J{\cdot}kg^{-1}{\cdot}K^{-1}$	400			
Melt production parameters						
Solidus surface temperature (model M2)	T_{S0}	°C	1090			
Damp solidus surface temperature (model M2)	T_{S0wet}	°C	890			
Solidus depth derivative (model M2)	$\left.\frac{\delta T_S}{\delta z}\right\|_X$	$K{\cdot}m^{-1}$	$3.4{\cdot}10^{-3}$			
Solidus depletion derivative (model M2)	$\left.\frac{\delta T_S}{\delta X}\right\|_z$	K	440			
Incremental batch melting coefficient (model M1)	ϕ/ϕ_{batch}	–	0.55			
Rheological parameters						
Effective viscosity range	μ_{eff}	Pa.s	$10^{18}-10^{27}$			
Strain weakening range	$\varepsilon_1-\varepsilon_2$	%	5 –105			
Angle of internal friction	ϕ_{eff}	°	15			
Strain weakened angle of internal friction	ϕ_{eff}	°	2 (4 in the mantle)			
Cohesion	C	MPa	20			
Strain weakened cohesion	C	MPa	4 (20 in the mantle)			
Dislocation creep flow laws parameters						
			UC	LC	CLM	SLM
Flow law	–	–	WQ	DIA	WO	WO
Scaling factor	f	–	1	0.1	5	1
Power law exponents	n	–	4	4.7	3	3
Activation energy	Q	$kJ{\cdot}mol^{-1}$	222.81	485	429.83	429.83
Power law constant	A	$Pa^{-n}{\cdot}s^{-1}$	$8.574{\cdot}10^{-28}$	$5.77904{\cdot}10^{-27}$	$1.758{\cdot}10^{-14}$	$1.758{\cdot}10^{-14}$
Activation volume	V	$m^3{\cdot}mol^{-1}$	0	0	$15{\cdot}10^{-6}$	$15{\cdot}10^{-6}$

Flow laws are based on power law with creep parameters from Gleason and Tullis (1995) for Wet Quartz (WQ), Karato and Wu (1993) for Wet Olivine (WO) and Mackwell et al. (1998) for Dry Diabase (DIA) Appendix A. UC = Upper-Crust, LC = Lower-Crust, CLM = Continental Lithospheric Mantle and SLM = Sub-Lithospheric Mantle.

$$\rho(T) = \rho_0(1-\alpha(T-T_0)) \quad (3)$$

where ρ_0 is the reference density and α the thermal expansion.

We define two types of models depending how the density structure and melt prediction in the mantle are calculated. In model M1, we use a lookup table approach where the density and the melt fraction are extracted from the thermodynamic calculation depending on pressure and temperature. This model intrinsically considers temperature and pressure dependent phase changes, thermal expansivity and compressibility in the mantle. Conservation of mass is approximated by the incompressible continuity equation with the extended Boussinesq approximation (Gerya, 2010). We also assume that phase changes with varying condition of pressure and temperature are quick enough to be considered as instantaneous during material advection. A depletion buoyancy term is added to the density read from the table outside the melt window when required in the mantle lithosphere. This is a correction related to the mantle depletion during melting beneath the mid oceanic ridge that we add to the density when the mantle leaves the melt window.

In model M2 the density of the mantle depends only on thermal expansion without considering phase changes following Eq. 3 and the melt prediction is based on a linearized solidus. In model M2 the reference density in the sub-lithospheric mantle is set to 3311 kg/m^3. This value is the calibrated reference mantle density that must be used to fit the elevation difference between continents and mid-ocean ridges. The calibration procedure is explained below.

4.2. Melt prediction and related feedback on mantle densities

In model M1, melt prediction is based on thermodynamic calculation using the characteristic fertile mantle composition SP2008 from Simon and Podladchikov (2008) (Fig. 6 and 7) The melting solution for dry conditions is calculated at equilibrium meaning that there is a mix of melt and solid in a closed system (batch melting) Appendix C. We use only one thermodynamic solution assuming a linear relationship between total melt fraction from batch melting and incremental batch melting. Calibration of this parameter to fit the predicted 6.5 km thick oceanic crust provides a value of $\phi/\phi_{batch} = 0.55$, consistent with earlier modeling (e.g., Hirschmann et al. (1998)) (Fig. S10). In model M1, mantle material produces additional melt only if the predicted melt fraction ϕ is higher than the highest melt fraction encountered during its history.

In model M2, melt prediction is based on a linearized mantle solidus (e.g., Lu and Huismans, 2021; Nielsen and Hopper, 2004; Scott, 1992; Simon et al., 2009) Appendix B. The linear mantle solidus approach is based on the parametrization by McKenzie and Bickle (1988) and is

justified since the solidus is almost linear up to pressures of approximately 4 GPa (120 km depth). The melt model considers depletion and the change of the solidus with increasing total melt fraction.

Melt prediction is coupled to the thermo-mechanical model through the use of the lithostatic pressure (model M1) or depth (model M2) and temperature. The model accounts for feedback from latent heat by melting on temperature, from melt weakening and dehydration strengthening on viscosity, and density Appendix D.

Feedback of melting on density is different for models M1 and M2. The feedback of melting on mantle density has two different effects: (1) Melt buoyancy ($\Delta\rho_m$) related to in situ melt retention *(Eq. 4)* (Scott and Stevenson, 1989) and *(2)* compositional or depletion buoyancy ($\Delta\rho_X$) related to progressive depletion of the melt source in heavy elements (Al, Ca, Fe, Si) with increasing total melt fraction (Oxburgh and Parmentier, 1977; Jordan, 1979; Afonso and Schutt, 2012; Schutt and Lesher, 2006). Melt buoyancy is computed similarly for model M1 and M2 except that in M1 the melt density is provided by the thermodynamic solution while model M2 uses a user-defined constant melt density, ρ_m so that maximum melt buoyancy is given by:

$$\Delta\rho_m = -(\rho_0 - \rho_m)\phi_{ret} \tag{4}$$

where ϕ_{ret} is the melt retention fraction in the residual. For model M2, the depletion buoyancy is computed using the following parametric relation:

$$\Delta\rho_X = -\frac{\rho_0 - \rho_{X_{ref}}}{X_{ref} - 1}\left(1 - \frac{1}{X}\right) \tag{5}$$

where X is the concentration of a perfectly compatible trace element, and $\rho_{X_{ref}}$ is the density of the residue at X_{ref} (Scott, 1992; Nielsen and Hopper, 2004).

For model M1, the depletion buoyancy is calculated using the thermodynamic solution at equilibrium for dry melting conditions. Similarly to the determination of the melt fraction it is theoretically not possible to directly use this solution to determine the density distribution inside the melt window or for mantle that experienced melt extraction. However, the thermodynamic solution for the density of the solid during melting does not exhibit phase change related density changes and is mostly a function of the melt fraction and mantle potential temperature (Fig. 6a and supplemental Fig. S12). We also note that the reference density at the onset of melting, i.e. on the dry solidus, along the adiabat is almost constant, about 3396 kg/m^3 for mantle potential temperature lower than 1350 °C. We use this observation to define a self-consistent relationship between depletion buoyancy and increasing melt fraction assuming that the density of the residuum calculated at equilibrium is close to the one considering fractionation during melting (Fig. S12):

$$\Delta\rho_X = \begin{cases} -3.8\phi, & \text{if } \phi < 7.5 \\ -(24.84 + 0.488\phi), & \text{otherwise} \end{cases} \tag{6}$$

This relationship predicts about 1% density reduction for 20% melt extraction, in agreement with previous studies (Schutt and Lesher, 2006; Afonso and Schutt, 2012).

There is no solution to properly estimate density of mantle that went through the melt window using only one thermodynamic solution. We estimate the density of material that has gone through the melt window by tracking the maximum depletion buoyancy experienced during melting and apply this to the P-T dependent density of the fertile thermodynamic solution. This results in a small overestimation of the effect of the spinel to plagioclase phase transition on density. The depleted mantle exhibits a smooth density transition from garnet to spinel to plagioclase (Fig. 7) (Simon and Podladchikov, 2008). Just using one thermodynamic composition table results in a wide plagioclase domain with a reference density of about 3250 −3275 kg/m^3 when the hot and low-pressure mantle leaves the melt window while this domain should be characterized with a reference density of about 3300 kg/m^3 for a depleted mantle (Fig. 7). Adding a depletion buoyancy term to the mantle that went through the melt window enhances this effect resulting in an underestimate of the density increase with the cooling oceanic lithosphere away from the ridge. However, we show that this has a minor effect on MOR elevation which mostly depends on densities inside the melt window (see supplemental model SM1b on Fig. S15). We use the melt prediction to compute an average constant oceanic crustal thickness with a reference density at $T = 0$°C set to 2900 kg/m^3 which varies with temperature (Eq. 3). The oceanic crust is included in the model by applying a phase change to the oceanic sub-lithospheric mantle shallower than the predicted average oceanic crust thickness. When the mantle material reaches a depth relative to seafloor elevation lower or equal to the reference oceanic crustal thickness (~6 km), material color and density change to those of bulk oceanic crust material. Oceanic crust keeps the same rheology, i.e. fully frictionally weakened material to avoid strain localization (e.g., Theunissen and Huismans, 2022).

5. Thermo-mechanical modelling results

We first present results of the 2-D thermo-mechanical model M1 from continental rifting to steady state mid-ocean ridge (MOR) spreading and then compare this to results of model M2. These simulations predict the elevation and the density structure beneath the MOR. Model M1 is used as a reference and includes densities obtained from thermodynamic solutions. Model M2 uses densities that depend on thermal expansion and temperature only.

5.1. Model M1

Reference model M1 (Fig. 8) has mantle densities and melt prediction based on thermodynamic tables of the fertile mantle with composition SP2008 (Simon and Podladchikov, 2008) that provides a good match with geophysical observations for the Earth upper-mantle (Section 3, Fig. 6 and Table 2). M1 has a strong crustal rheology with a decoupling layer in the viscous mid crust. Deformation follows three phases: 1) upper-crustal and upper-mantle normal faulting and viscous necking, 2) distal margin formation and lithosphere breakup, and 3) seafloor spreading. Phase 1 (0–2.7 Ma) (see supplementary video M1 for full time evolution) results in a highly asymmetric graben. Phase 2 (2.7–4 Ma) exhibits crustal necking coupled with the buoyant and hot exhuming sub-lithospheric mantle resulting in efficient crustal thinning and lithospheric breakup at 4 Ma. Partial melting starts at the beginning of phase 2 at about 2.5 Ma. We observe melt addition in the distal margin and a sharp transition to normal oceanic crustal thickness. A steady-state oceanic spreading center (phase 3), with production of a stable and constant thickness oceanic crust of 6.5 km, is established soon after lithospheric breakup. The mid-ocean ridge is at −2742 m below sea level while the elevation of the stable continental lithosphere (top of the model) is at +400 m. At 17 Ma, after 12.2 Myrs of active spreading, the oceanic seafloor has an elevation of −3000 m below sea level at the continent-ocean boundary.

5.2. Model M2

Reference model M2 (Fig. 9) only differs from model M1 in the way lithospheric and sub-lithospheric mantle densities and melt prediction are calculated using the classical Boussinesq approximation considering only the effect of constant thermal expansion on densities, and melt prediction based on a linearized solidus (e.g., Section 4.2 and Appendix B). The overall model evolution is similar to model M1 with some small differences. Phase 1 initial graben formation (0–2.5 Ma) is slightly shorter than in model M1. Phase 2 distal margin formation and lithospheric breakup is similar to model M1 and leads to a time of breakup of about 4.1 Ma. Phase 3 steady-state spreading results in production of stable oceanic crust with a thickness of 6.5 km soon after lithospheric

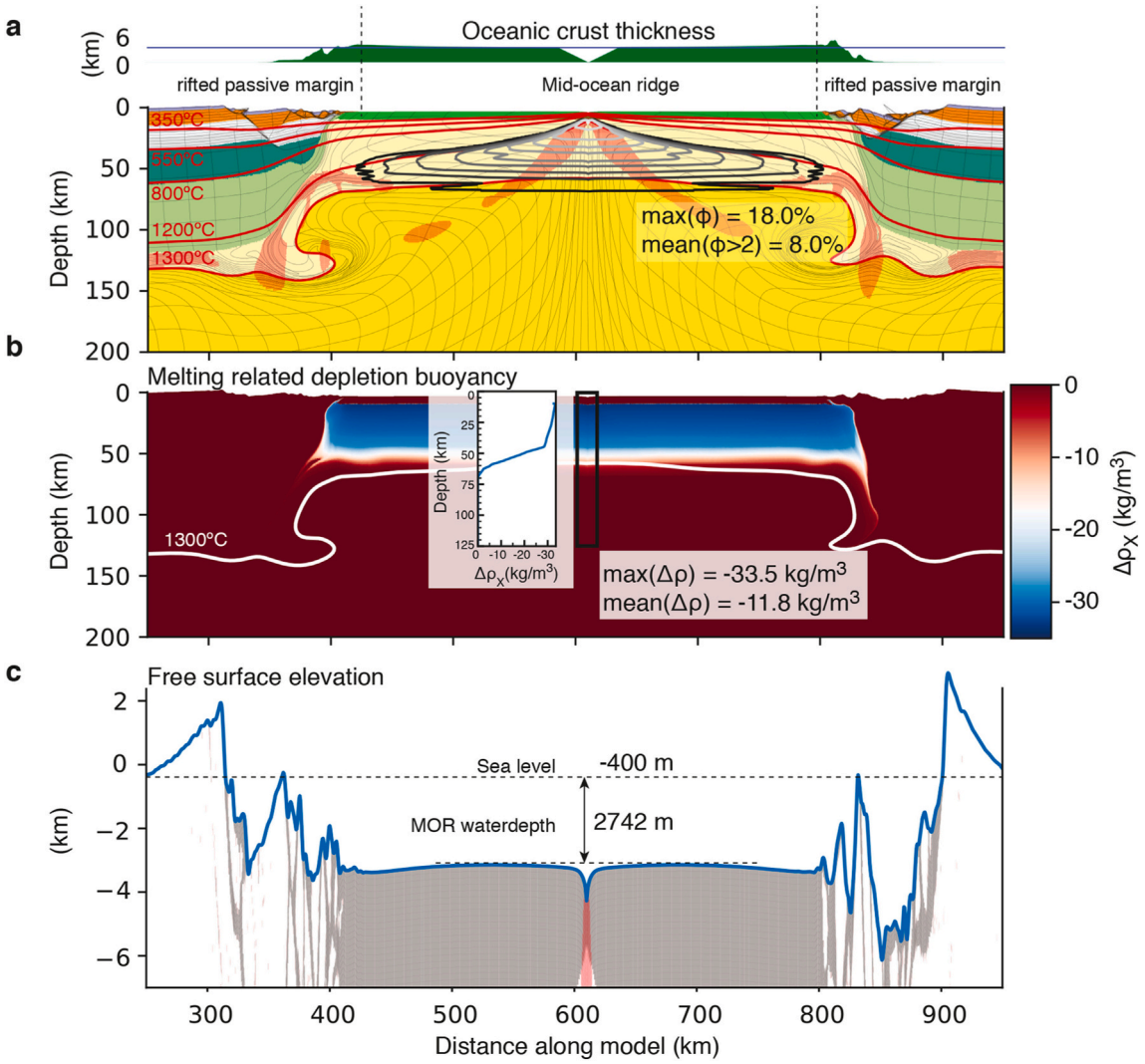

Fig. 8. Snapshot of model M1 after 17 Myrs of extension including 12 Myrs of seafloor spreading at 3 cm/yr full spreading rate. Mantle density and melt prediction are from the thermodynamic solution using fertile mantle composition SP2008 (see Tables 1 and 2 and Fig. 6). The average predicted oceanic crustal thickness between the two rifted conjugate passive margins is 6.5 km. Gray color represents plastic strain weakened areas; red color represents areas with strain rate higher than 10^{-14} s^{-1}.

breakup. The mid-ocean ridge is at an elevation of −2743 m below sea level while the stable continental lithosphere (model top) is at +400 m above sea level. At 17 Ma, after about 12 Myrs of active spreading, the elevation of the oceanic seafloor reaches −3550 m at the continent-ocean boundary.

5.3. Model comparison

Models M1 and M2 represent two simulations among many models that we have run. For the parameters in these models the predicted elevation difference between the mid-ocean ridge and the stable continental lithosphere provides a good fit with values observed on Earth (e.g., Section 2). However we note that the predicted elevation difference is highly sensitive to the value of the crustal density and the degree of depletion of the lithospheric mantle. For example using a depletion buoyancy of zero in the continental lithospheric mantle in model M1 results in a mid-ocean ridge depth of 2350 m below sea level with a continent at +400 m elevation (e.g., Supplemental Fig. S15). Considering M2, using the same reference density for the continental lithospheric mantle and the sub-lithospheric mantle of 3300 kg/m^3, as is very common in geodynamic models, results similarly in a mid-ocean ridge depth that is 2210 m below sea level, much smaller than observed. We also note that supplementary model SM2b, equivalent to model M2 without melt prediction and associated related feedback on density and that uses the same reference density for the continental lithospheric mantle and the sub-lithospheric mantle of 3300 kg/m^3, results in an over-estimated mid-ocean ridge water depth of 3 km assuming a 6.5 km thick oceanic crustal layer on top, and of 4.2 km MOR depth assuming no oceanic crust (e.g., Supplemental Fig. S15).

5.4. Sensitivity to spreading rate

We next test the sensitivity of mid-ocean ridge elevation on spreading rate for model setup 1 and 2 (Fig. 11). At full spreading rates higher than 2 cm/yr, MOR elevation and magmatic production are approximately constant, respectively −2750 m and 6.5–7 km, in agreement with observations. At low spreading rates magmatic oceanic crustal thickness decreases rapidly, associated with progressive increasing of the MOR water depth from 3100 m at 1 cm/yr to limit values of 3400 m at 0.75 cm/yr full spreading rate. This is consistent with observations made on Earth where average elevation decreases to about −3100 m and −3300 m at respectively 1 cm/yr and 0.75 cm/yr full spreading rates (Fig. 2).

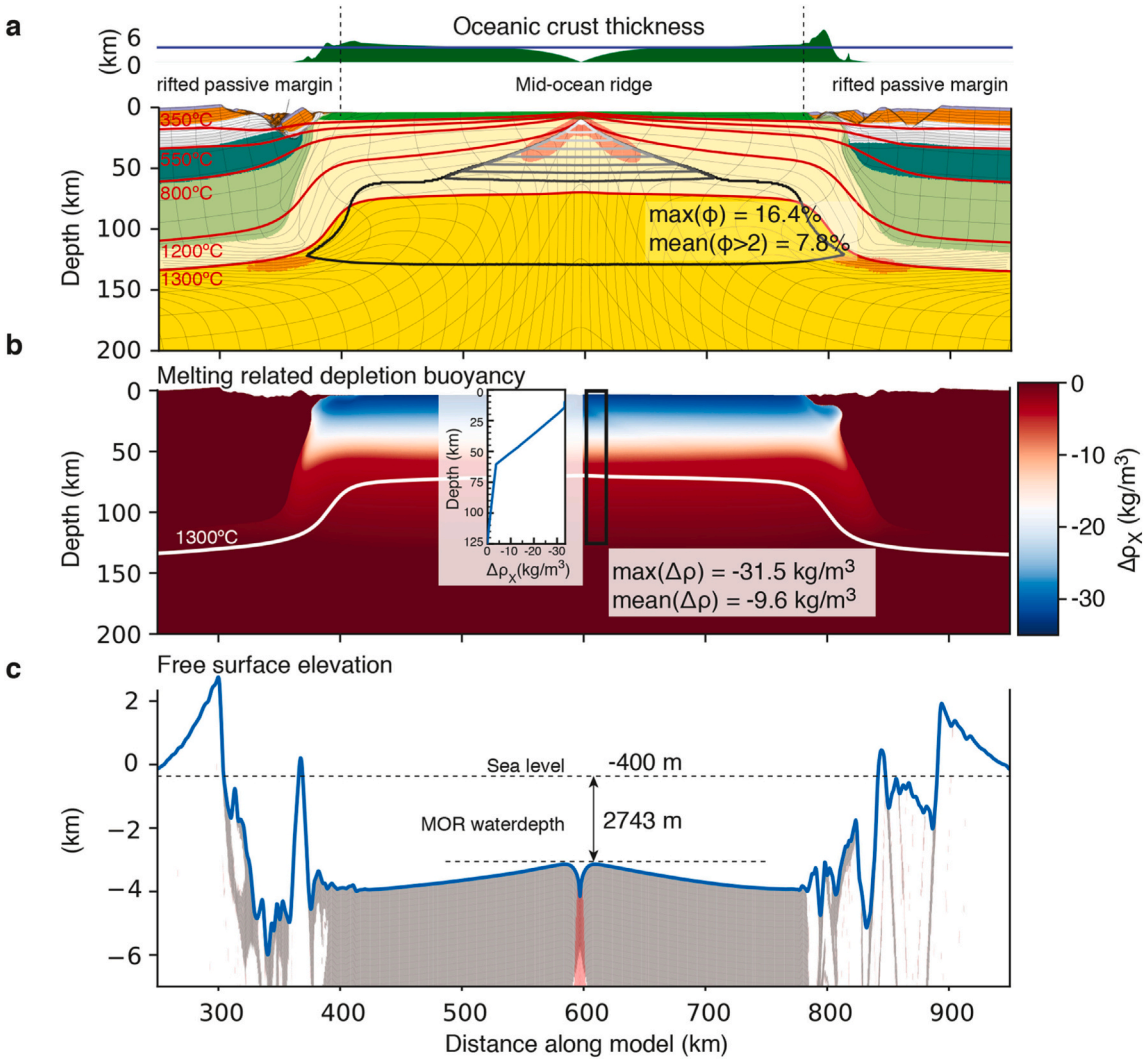

Fig. 9. Snapshot of model M2 after 17 Myrs of extension including 12 Myrs of seafloor spreading at 3 cm/yr full spreading rate. Constant reference mantle density with thermal expansion and melt prediction using linearized mantle solidus. The average predicted oceanic crustal thickness between the two rifted conjugate passive margins is 6.5 km. Gray color represents plastic strain weakened areas; red color represents areas with strain rate higher than 10^{-14} s^{-1}.

6. 1-D calibration of crustal and mantle densities

The 2-D models demonstrate that the choice of the reference densities of the crust, the continental lithospheric mantle, and the sub-lithospheric mantle control the elevation difference between stable continental lithosphere and the mid-ocean ridge. Here we calibrate the density structure of two 1-D reference columns against the observed elevation difference between active mid-ocean ridges and stable continents assuming local isostatic compensation (Fig. 1 and Table 4). First we define the two reference columns. We then establish the density structure of the mid-ocean ridge and use this as a reference to obtain the elevation difference with a column of continental lithosphere for varying crustal density and lithospheric mantle depletion.

Table 4
The two reference columns for Earth as defined in this study.

Reference MOR column	
Full-spreading rate	3 cm/yr (active spreading)
Distance to any hotspots	>1000 km
Oceanic crustal thickness	6.5 km
Elevation	$-2750 \pm 250m$
Reference continental column	
crustal thickness	35 km
lithospheric thickness	125 km
Approximate age	Early Phanerozoic
strain rate	$\dot{\varepsilon_H} < 10^{-16} s^{-1}$ (stable)
Distance to any hotspots	>1000 km
Elevation	$+ 400 \pm 400m$

6.1. Definition of two reference columns

The main reference column is representative of the active MOR far from hotspots with full spreading rates higher than 2 cm/yr (Fig. 2). For the oceanic crust, we use a reference thickness of 6.5 km and a reference density of 2900 kg/m^3 that results in an average oceanic crustal density of $\sim$ 2875 kg/m^3 at the MOR considering the effect of thermal expansion, in agreement with global estimates (e.g., Carlson and Raskin, 1984; Tenzer and Chen, 2019). For the mantle, we use the density as a function of depth at the spreading mid-ocean ridge extracted from the 2-D thermo-mechanical model M1 that is coupled to the thermodynamic solution based on the reference fertile mantle composition SP2008. Below the oceanic crust three domains can be distinguished (Fig. 10a). A 4 km thin layer with low density $\sim$ 3100 kg/m^3 dominated by plagioclase, a second 55 km thick domain representing the melt window below the ridge where density slowly increases with depth and with decreasing

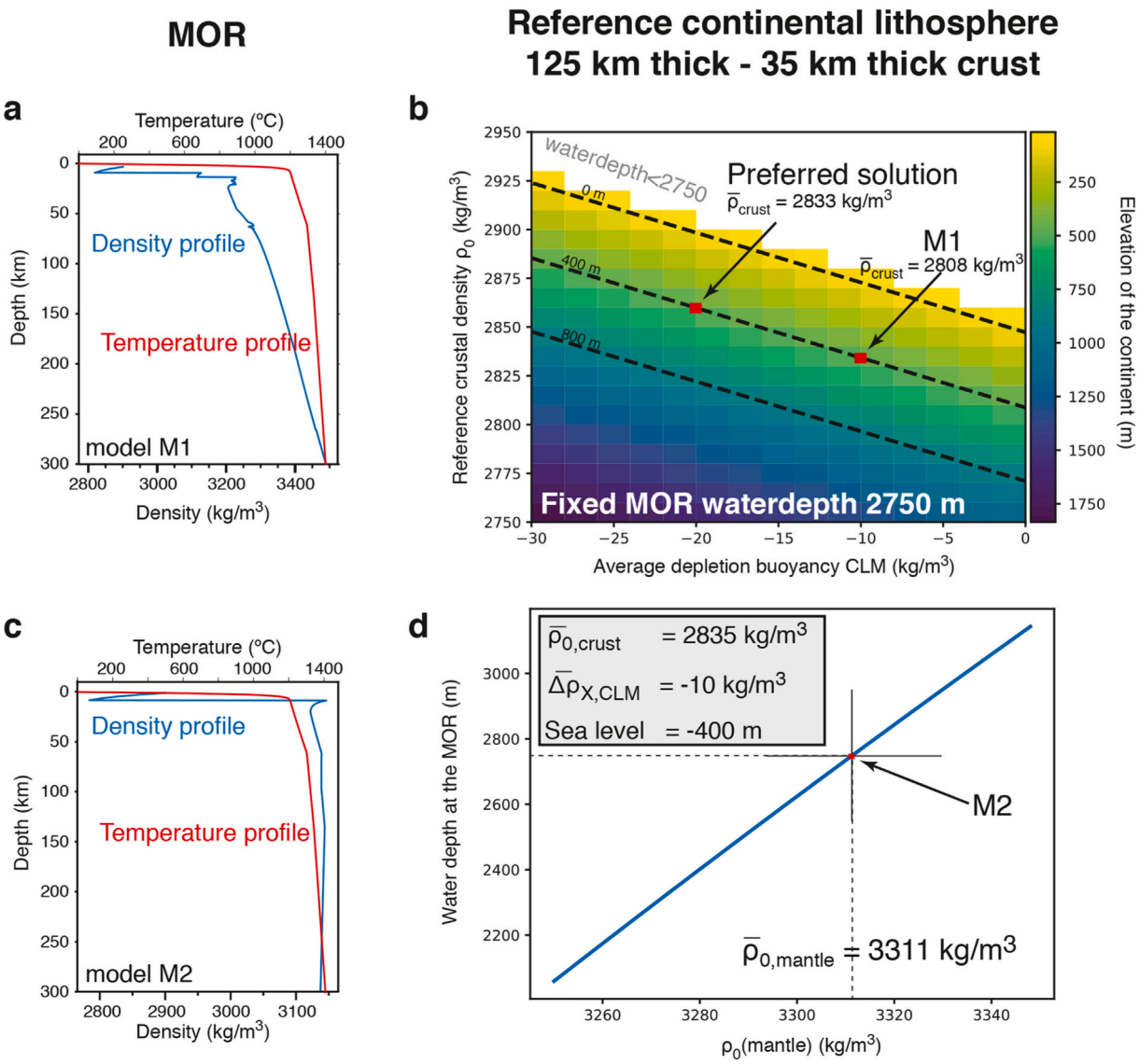

Fig. 10. 1-D calibration of the relative elevation between continent and MOR. A compensation depth of 125 km is used in the 1-D local isostatic calculations (Fig. 1 and Eq. 7). **a**, density structure at the MOR from model M1. Note that model density includes the effect of compressibility. **b**, 1-D isostatic calibration and calibration of the average crustal density and the average depletion buoyancy of the reference 125 km thick Phanerozoic continental lithosphere to fit the elevation of the continent. **c**, density structure at the MOR from model M2. Note that model density only includes the effect of temperature through thermal expansivity. **d**, knowing the average crustal density 2835 kg/m^3 and the average depletion buoyancy of the CLM −10 kg/m^3 from (b,) the 1-D isostatic calculation provides the reference density of the sub-lithospheric mantle in model M2.

melt fraction toward the base of the melt window and, below that a domain that exhibits quasi-linear increasing density with depth along the adiabat. The average depletion buoyancy of the mantle between the base of the oceanic crust and a depth of 125 km beneath the MOR resulting from melt extraction is −11.8 kg/m^3 with a maximum of ~ −33.5 kg/m^3 at the top of the melt window (Fig. 8b).

The second column represents stable continental lithosphere far from hotspots (Fig. 4). We use a reference continental crustal thickness of 35 km (e.g, Fig. 5 and a reference lithospheric thickness of 125 km, representative of Phanerozoic lithosphere (Artemieva, 2006) (e.g., Section 2 and Fig. 5d). For the crust we assume that the density only depends on thermal expansivity for a given reference density at 0°C. For the continental mantle lithosphere we assume that the density variation with depth is controlled by the fertile mantle composition offset by a constant density contrast resulting from depletion. We use a 1-D analytical solution of the steady-state geotherm that reflects average values for Phanerozoic continental lithosphere (Table 3) (Hacker et al., 2015) to compute the density distribution as a function of depth by reading the P-T dependent density maps of the reference fertile mantle composition also used for the oceanic lithospheric column. The density variation with depth for crustal reference density of 2835 kg/m^3 and a continental mantle lithosphere depletion buoyancy $\Delta\rho_X = -10$ kg/m^3 (values used in model M1) is shown in Fig. 10a.

6.2. 1-D calibration procedure

We next use the density structure of the two reference columns to compute their elevation difference assuming local isostatic compensation at a depth of 125 km. We compute the 1-D lithostatic pressure for these two columns including the water load on top of the oceanic column. We determine the continental lithospheric thickness H_{cont} that provides a pressure equal to the pressure for the MOR reference column at the compensation depth. The difference in column height gives the total elevation difference between the continent and the MOR following:

$$h_{cont} + W = H_{cont} - H_{ridge} \quad (7)$$

where h_{cont} is the elevation of the continental column, W the water depth at the mid-ocean ridge, H_{cont} the thickness of the continental column and H_{ridge} the thickness of the MOR column (Fig. 1). H_{cont} is the lithospheric thickness and corresponds to $H_L + h_{cont}$, while H_L is the lithospheric thickness relative to sea level (Fig. 1). H_L is fixed at 125 km which is the compensation depth in our calculations.

For consistency, we compare the analytical solution to the difference in elevation predicted by the 2-D thermo-mechanical model using the same reference densities, composition and depletion. The two solutions exhibit a small difference that is caused by secular cooling of the continental lithosphere in the 2-D model as compared to the 1-D thermal steady-state analytical solution and by the effect of dynamic pressure deviating from the lithostatic pressure in the 2-D model Appendix D. In order for the 1-D analytical computation to reproduce the elevation difference in the 2-D thermo-mechanical model a very small correction of -0.4 kg/m^3 in the MOR mantle is required. At this stage, the 1-D analytical solution based on the two reference columns (Table 4) can be used to test the sensitivity of the elevation difference between continent and MOR to continental crustal density and to the depletion buoyancy of the continental lithospheric mantle.

6.3. Results of the 1-D calibration of crustal and mantle densities

We now vary both the reference crustal density $\rho_{0,crust}$ and the continental mantle lithosphere depletion buoyancy $\Delta\rho_{X,CLM}$ systematically to compute the continental elevation h_{cont} assuming a water depth of $W = 2750$ m on top of the mid-ocean ridge column (Fig. 10b). Continental elevation varies linearly with crustal density and average depletion buoyancy of the CLM. The resulting contour for 400 m continental elevation shows a trade-off between crustal density and continental mantle lithosphere depletion buoyancy. The values used in model M1 for reference crustal density ($\rho_{0,crust} = 2835$ kg/m^3) and continental mantle depletion ($\Delta\rho_{X,CLM} = -10$ kg/m^3) illustrate the match of the continental elevation between 2-D model prediction and analytical solution (Fig. 10b). We also indicate the 0 m and 800 m contours for continental elevation as this shows the domain with permissible elevations for observed Phanerozoic lithosphere with a crustal thickness of 35 km (Fig. 5). Model M1 ($\rho_{0,crust} = 2835$ kg/m^3 and $\Delta\rho_{X,CLM} = -10$ kg/m^3) does fit the water depth 2750 m at the MOR and the average elevation $+400$ m of the reference continental column. We note that a depletion buoyancy of -10 kg/m^3 is in agreement with the average depletion buoyancy calculated using the bulk composition YLM2 characteristic of a Phanerozoic lithosphere (Table 2).

We use the calibrated average continental crustal density and depletion buoyancy based on the thermodynamic consistent approach above to establish the reference densities that can be used for continental mantle lithosphere and sub-lithospheric mantle in models that follow the classic Boussinesq approximation where density depends on thermal expansivity. Assuming a reference crustal density of $\rho_{0,crust} = 2835$ kg/m^3, a characteristic mantle lithosphere depletion of -10 kg/m^3 and a continental elevation of 400 m allows computing a reference density ρ_0 for the sub-lithospheric mantle of ~ 3310 kg/m^3 at 0°C (Note that the actual continental mantle lithosphere reference density $\rho_{0,CLM}$ is offset by the depletion buoyancy $\Delta\rho_{X,CLM}$ as $\rho_{0,CLM} = \rho_0 - \Delta\rho_{X,CLM} = 3300$ kg/m^3) (Fig. 10d).

7. Discussion

The combined results from 2-D thermo-mechanical and 1-D isostatic calculations show that the relative elevation difference between mid-ocean ridges and continents depends on crustal density, mantle composition and density distribution, and the degree of depletion of the lithospheric mantle in the reference case (35 km thick continental crust and 85 km thick continental lithospheric mantle). The use of self-consistent thermodynamic calculations allows the calibration of mantle densities beneath the mid-ocean ridge and in the lithospheric mantle. We will next make a comparative analysis of models M1 and M2. We will then discuss the variability of crustal and mantle densities by comparing with other independent estimates and by calculating the influence of changes in the temperature structure and lithosphere thickness. We will finally discuss limitations of the approach developed in this study.

7.1. Toward a calibration of reference mantle densities in geodynamic modelling

Model M2 that is based on the classical Boussinesq approximation where density only depends on temperature is used to calibrate the reference density of the mantle to fit the characteristic elevation difference between stable continents and mid-ocean ridges (Fig. 10c and d). Combined results from geodynamic model M1 where mantle densities are constrained by thermodynamic calculations (Fig. 8 and 1-D isostatic calculations (Fig. 10b) show that the average crustal density $\overline{\rho}_c$ and continental mantle lithosphere depletion that fit the observed elevation difference between 125 km thick stable Phanerozoic continental lithosphere with a 35 km thick crust at $+400$ m elevation and mid-ocean ridge at 2750 m water depth follow this relation:

$$\overline{\rho}_c = -2.5\overline{\Delta\rho}_{X,CLM} + 2783 \quad (8)$$

where $\overline{\rho}_c$ is the average crustal density, $\overline{\Delta\rho}_{X,CLM}$ the average depletion buoyancy of the continental lithospheric mantle, and a reference density of the sub-lithospheric mantle ~ 3310 kg/m^3 at 0°C (See also supplemental Fig. S14). We note that this dependency includes mantle depletion through melting beneath the mid-ocean ridge with values consistent with those from thermodynamic calculations (e.g., Figs. 8b and 9b). Without considering mid-ocean ridge melting but including 6.5 km thick oceanic crust such as in model M2, would require a lower reference mantle density 3275 kg/m^3 at 0°C to fit the elevation difference between stable continents and MOR (See also supplemental Fig. S15).

7.2. Average crustal densities and CLM depletion buoyancy

Gravity inversion, conversion from seismic wave velocity, and global joint inversion are commonly used to assess the density structure in the Earth (Afonso et al., 2019; Fullea et al., 2021; Christensen and Mooney, 1995; Zoback and Mooney, 2003; Tenzer et al., 2015; Hasterok and Chapman, 2007; Karabulut et al., 2019; Artemieva, 2019; Globig et al., 2016). Based on global seismological datasets average continental crustal density is estimated to ~ 2835 kg/m^3 for a typical 35–40 km thick continental crust (Christensen and Mooney, 1995; Zoback and Mooney, 2003; Tenzer et al., 2015). Regional studies and seismological inversions indicate a high variability of crustal density around the mean value with a range [2750 −2900] kg/m^3 (Hasterok and Chapman, 2007; Karabulut et al., 2019; Artemieva, 2019; Globig et al., 2016; Crosby et al., 2010; Fullea et al., 2021) (Table 6). We note that average crustal density increases with crustal thickness (Zoback and Mooney, 2003; Artemieva, 2019). Here, however, we restrict ourselves to stable continental areas with average crustal thickness ~ 35 km and elevations $+400 \pm 400$ m (Fig. 5).

We use a reference crustal density of 2835 kg/m^3 at 0°C. Density in the crust in our models only depends on temperature (Eq. 3) and the average continental crustal density for models 1 and 2 is therefore 2808 kg/m^3 (Table 5). Our results show that this crustal density requires a continental mantle depletion buoyancy of -10 kg/m^3 (Fig. 10 and Eq. 8). Using an average continental crustal density consistent with the global average (2833 kg/m^3) requires a depletion of -20 kg/m^3 to fit the elevation difference between MOR and continents (Table 5). We note that a depletion buoyancy of -20 kg/m^3 is in agreement with the

Table 5
End-members values for the average continental crust density from modeling results.

$\overline{\rho_c}$ kg/m^3	$\overline{\Delta\rho_{X,CLM}}$	$\overline{\rho_0}(\alpha)$	$\overline{\rho_0}(\alpha,\beta)$
2808	−10	2835 (M1 and M2)	2821.5
2823	−16	2850	2837
2833	−20	2860	2846
2850	−27	2877.5	2864
2902	−48	2930	2917

The last column provides the corresponding average reference density when combining the effect of temperature and pressure on density with depth (here we use constant compressibility of 10^{-11} Pa^{-1}). Models M1 and M2 are calibrated using the lowest estimate of the average crustal density. The end-member depletion buoyancy of −20 kg/m^3 also provide a reasonable average continental density in agreement with global estimates (Table 6). The last row ($\overline{\rho}_c$ = 2902 kg/m^3) results in an overestimation of the depletion buoyancy of the reference Phanerozoic CLM ($\overline{\Delta\rho}_{X,CLM} = -48 \ll -20$ kg/m^3) based on results of thermodynamic calculations.

Table 6
A selection of calculated average crustal density on Earth.

$\overline{\rho_c}$ kg/m^3	Type	Reference
2835	Global - Velocity waves conversion to density	Christensen and Mooney (1995)
2837	Global - Velocity waves conversion - Regression with crustal thickness	Zoback and Mooney (2003)
2830	Global - Crust1.0	Tenzer et al. (2015)
2846	Regional - North America - Velocity waves conversion to density	Hasterok and Chapman (2007)
2850	Regional - Anatolian-Aegean - Inversion of the density contrast at the Moho and Pn waves conversion to density	Karabulut et al. (2019)
~ 2820	Regional - European - Seismic waves conversion and thermal isostasy	Artemieva (2019)
2790	Regional - Africa - Local isostasy with little care of mantle densities	Globig et al. (2016)

average depletion buoyancy calculated using the bulk composition YLM3 characteristic of a Phanerozoic lithosphere (Table 2). Using the upper-bound of inferred average continental crustal density (~ 2900 kg/m^3) requires a depletion of −48 kg/m^3 which is significantly higher than the average depletion buoyancy inferred from characteristic Phanerozoic bulk mantle compositions based on thermodynamic calculations (e.g., Table 2).

7.3. Average depletion buoyancy of the CLM

We compute continental mantle depletion buoyancy required to fit the elevation difference for varying lithosphere thickness using a 125 km thick lithosphere column, with an average crustal density of 2833 kg/m^3 and depletion −20 kg/m^3 as a reference. Assuming the same reference crustal thickness and density among different tectonic terranes, the average depletion buoyancy required to fit the observed elevation difference between ridge and stable continent increases with increasing lithosphere thickness (Fig. 12 and 13). A lithosphere thickness in the range [140 −180] km, typical for Proterozoic areas (Artemieva, 2006), requires average mantle depletion in the range [−27; −37] kg/m^3, while a 280 km thick lithosphere requires an average depletion of about $\Delta\rho_X = -50$ kg/m^3 with a lower limit of −53.5 kg/m^3 (Fig. 12). We note that the variation of continental mantle lithosphere depletion buoyancy is consistent with our thermodynamic computed densities for mantle lithosphere composition of varying age (Table 2).

Composition and depletion buoyancy of the CLM may vary with depth (Gaul et al., 2000; Afonso et al., 2008; O'Reilly and Griffin, 2006; Griffin et al., 2008; Forte and Perry, 2000; Artemieva, 2009). For Archean terranes with 280 km thick lithosphere, Afonso et al. (2008) provided a good fit to the elevation and geoid using a layered continental mantle lithosphere with composition that varies with depth: 120 km thick upper-mantle lithosphere with ALM0 composition, 90 km thick mid lithospheric mantle layer with ALM2 composition, and 30 km lower lithospheric mantle with YLM2 composition (Table 1). Converting this layered density distribution to an average mantle lithosphere depletion gives $\Delta\rho_X = -53.5$ kg/m^3 which is consistent with the maximum average depletion found here for 280 km thick lithosphere (Fig. 12). We note that the average depletion buoyancy of the continental lithospheric mantle with models that only depend on temperature and that do not include phase changes is slighty higher for thicker lithospheres than with models that are coupled with thermodynamic calculations (Fig. 12a and 13). Fig. 13 shows the resulting density structure for three characteristic continental lithospheric columns (Phanerozoic, Proterozoic, Archean) and for a typical mid oceanic ridge column calibrated with the observed elevation difference between stable continental lithosphere and a mid oceanic ridge, which can directly be used in modeling.

7.4. Variability of MOR/continent elevations

Average elevation of stable continents characterized by a crustal

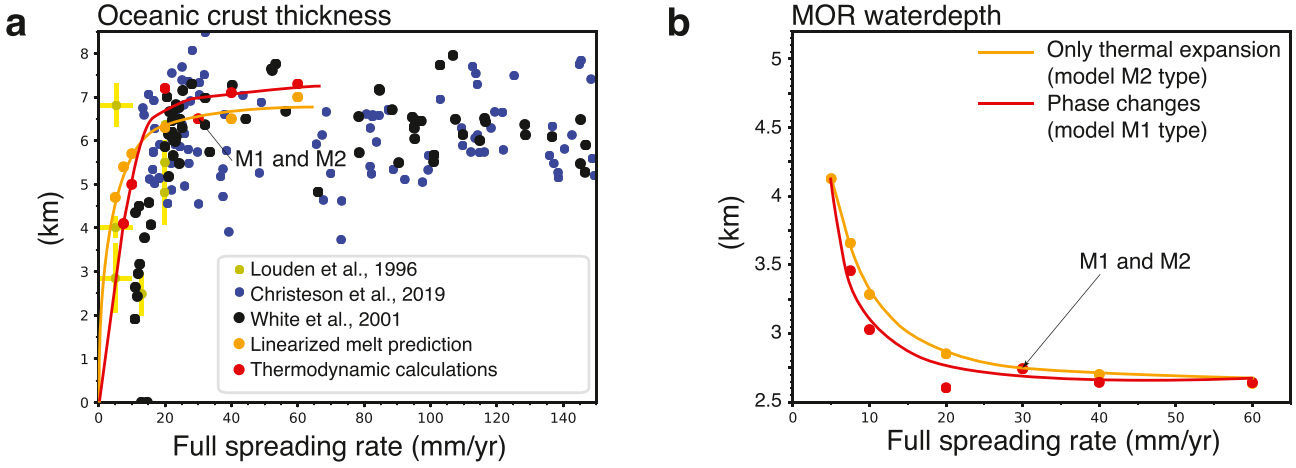

Fig. 11. Melt prediction models with respect to spreading rate. M1 (red) and M2 (orange). **a**, comparison of ocean crustal thickness from our models with observations from Louden et al. (1996); Christeson et al., 2019; White et al., 2001. **b**, water depth at the MOR versus spreading rate in our models.

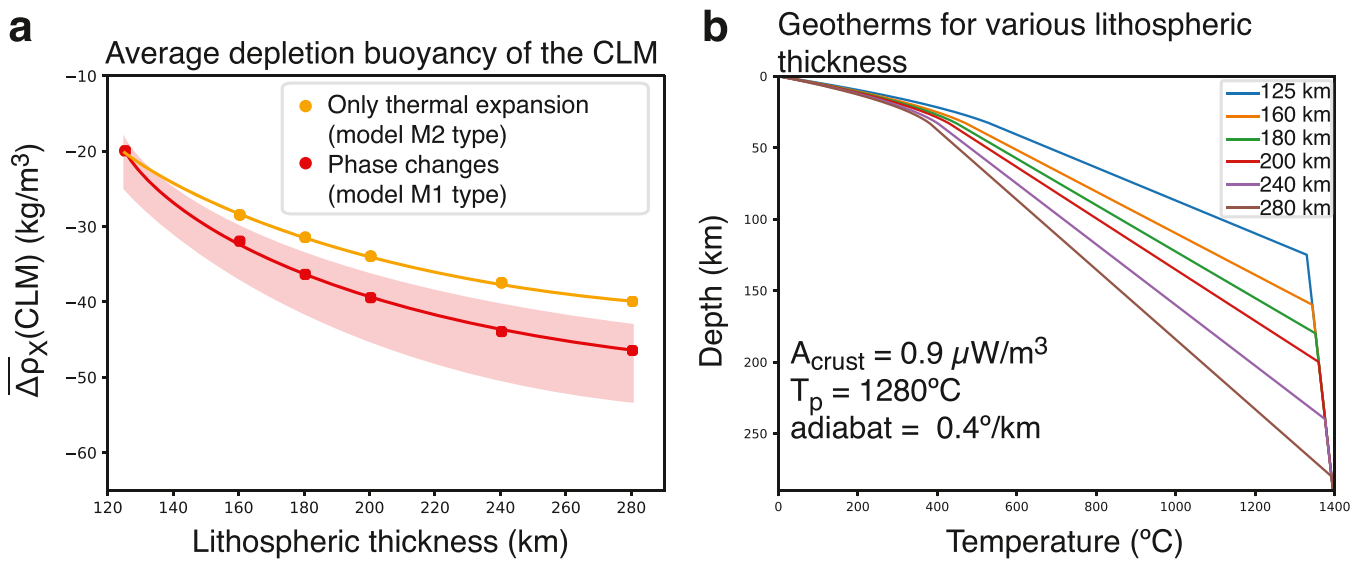

Fig. 12. 1-D computation of the average depletion buoyancy $\Delta\rho_X$ of the CLM for different lithosphere thickness. **a**, All 1-D continental lithospheric columns fit the same continental elevation +400 m and the same water depth at the MOR 2750 m. We use here the end-member $\rho_{0,crust}$ = 2860 kg/m^3 and $\Delta\rho_{X,CLM}$ = −20 kg/m^3 in the initial 125 km thick reference column because it provides a good fit to global average continental crust density about 2835 kg/m^3 and is in agreement with the depletion buoyancy calculated for the bulk composition YLM3. The orange curve uses density structure from model type M2 (constant thermal expansion). The red curve uses density structure from model type M1 where the depletion buoyancy is applied to the reference densities read in the thermodynamic P-T density tables. When using thermodynamic calculations (red curve), the average depletion buoyancy of the CLM depends on the bulk composition. The red curve uses the fertile SP2008 composition characteristic of the sub-lithospheric mantle corrected from the depletion buoyancy. The red shaded area corresponds to results using other bulk compositions provided in this study (Table 1). **b**, geotherms used to compute the 1-D isostatic calculation. Heat flow varies from 51 mW/m^2 to 41 mW/m^2 and Moho temperature varies from 550 °C to 390 °C respectively for lithospheric thickness from 125 to 280 km.

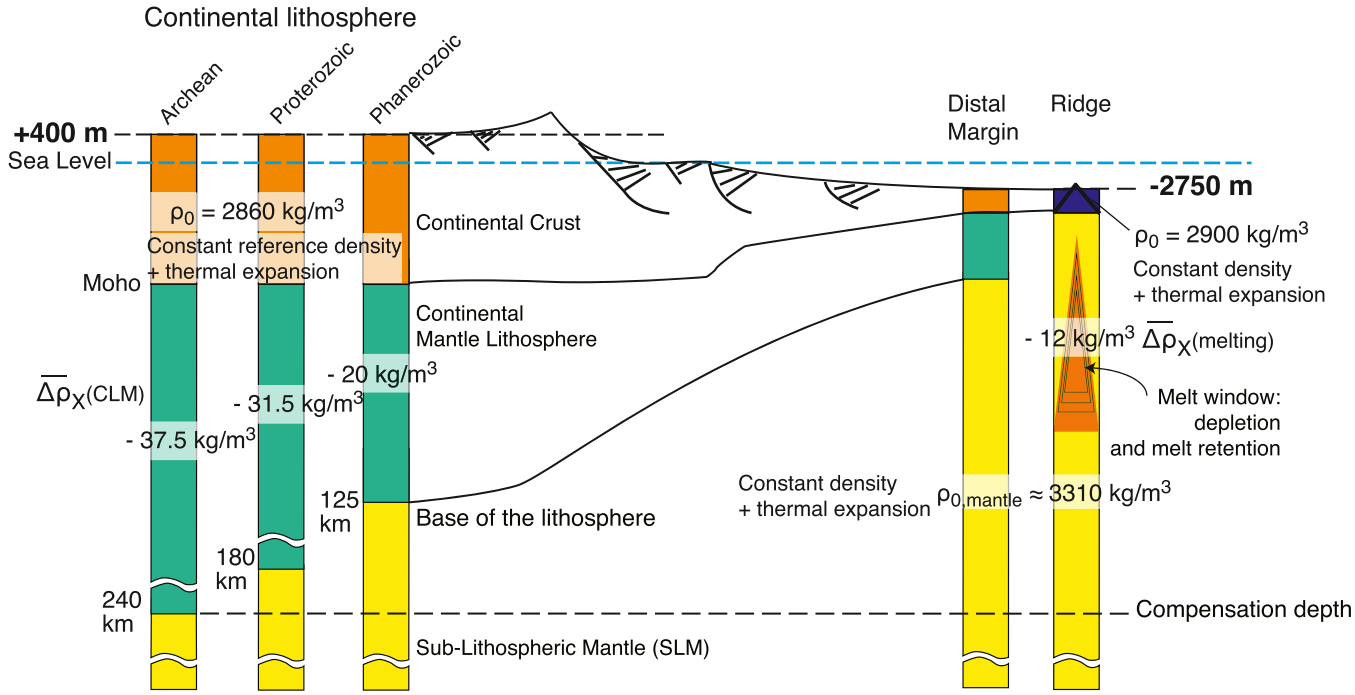

Fig. 13. Reference crustal and mantle densities calibrated to fit the relative continent/mid-ocean ridge elevation in agreement with geophysical and thermodynamic observations. The reference densities and the depletion buoyancy of the CLM for various lithospheric thickness given here corresponds to model M2 where densities only depend on temperature similarly to the orange curve in Fig. 12a.

thickness of 35 ± 5 km is as shown +400 ± 400 m (Figs. 4 and 5). The results from the 1-D isostatic calculations show that the variability in elevation can be explained by a variation in either crustal density or mantle depletion buoyancy in the reference case (35 km thick continental crust and 85 km thick continental lithospheric mantle). A difference in crustal density of ±35 kg/m^3 for a fixed depletion buoyancy in the CLM or a difference of ±15 kg/m^3 of the depletion buoyancy in the CLM for a fixed crustal density can explain a variability of ±400 *m*

(Fig. 10). Alternatively, variations of the temperature distribution in the lithosphere may lead to crustal and mantle density variations. A difference in Moho temperature of 100°C results in a change of the average crustal density of 5 kg/m^3 and an average CLM density difference of 5 kg/m^3 and corresponds to half of the variability of continental elevation, i.e. about 200 m. These variations in Moho temperature, crust and mantle densities are within the uncertainty of values expected on Earth (Jaupart et al., 2016; Christensen and Mooney, 1995; Zoback and Mooney, 2003; Tenzer et al., 2015; Artemieva, 2019; Griffin et al., 1999; Gaul et al., 2000; Afonso et al., 2008; O'Reilly and Griffin, 2006; Griffin et al., 2008; Lamb et al., 2020; Crosby et al., 2010).

Average elevation of active mid-ocean ridges far from hotspots is as shown -2750 ± 250 m (Fig. 2). MOR water depth is well reproduced by our results for full spreading rates in the range [0.75–6] cm/yr (Fig. 11). We do not explain the enigmatic higher water depth ($\sim$ 3000 m) for full spreading rates higher than 9 cm/yr (Fig. 2). We suggest that this may be the result of highly efficient hydrothermal cooling and complex interaction of the top of the melt window with the oceanic crust at the ridge axis both not included in our modelling approach (e.g., Crameri et al., 2019; Li et al., 2017; Grose and Afonso, 2013). The results from geodynamic modelling coupled with melt prediction also show that the variability in elevation of mid-ocean ridges depends on the extend of melting which is controlled by spreading rate, mantle temperature, and mantle source composition. While we focus here on a reference case representative of all mid-ocean ridges far from hotspots, the small variations in elevation of normal ridges ($\pm$250 m) can probably be explained by differences of the degree of melting, the melt source depletion and associated buoyancy, and of oceanic crust thickness caused either by small mantle temperature variations or by sub-ridge mantle compositional variations leading to different solidus (e.g., Liu et al., 2008; Liu et al., 2022; Niu, 2017; Niu, 2021). The anomalous case of hotspots that include much larger temperature variations is discussed in the next sections.

The postrift subsidence characteristics of model M2 match well with that predicted by half-space cooling models for oceanic lithosphere and are in agreement with global subsidence of the ocean floor with an elevation of -3600 m after 12 Ma of oceanic spreading (Fig. 9) (e.g., Crameri et al., 2019; Richards et al., 2018, and references therein). In contrast model M1 exhibits less subsidence as a function of age, i.e. -3000 m after 12 Ma of oceanic spreading (Fig. 8). This is caused by a limitation in our approach for model 1, where the buoyancy of the cooling oceanic lithosphere includes both the phase changes associated with fertile mantle composition and the depletion buoyancy owing to melting. While the predicted water depth at the mid-ocean ridge is correct, the model overestimates the buoyancy of the oceanic lithosphere outside of the melt window away from the ridge (See supplemental model SM1b on Fig. S15).

7.5. Mantle potential temperature

Our model is calibrated using a mantle potential temperature of 1280 °C, in the range of current estimates on Earth. Mantle potential temperatures can be inferred from petrological and geochemical studies of erupted lavas in mid-ocean-ridge and volcanic islands (e.g., Abbott et al., 1994; Herzberg et al., 2007; Kojitani and Akaogi, 1997; Matthews et al., 2021) and also based on indirect geophysical observations and modeling (e.g., McKenzie and Bickle, 1988; Dalton et al., 2014; Richards et al., 2018; Grose and Afonso, 2013). Hotspots in the mantle convection system are partially responsible for the variability of mantle potential temperature. However, recent independent studies suggest that mantle potential temperature for mid-ocean ridges far from hotspots, can be constrained to a narrow range 1300 ± 50°C (Fullea et al., 2021; Presnall et al., 2002; Dalton et al., 2014; Richards et al., 2018; Grose and Afonso, 2013; Cammarano and Guerri, 2017). A different choice in mantle potential temperature in our models would have limited effects because the melt production is calibrated to fit present day geophysical observations, implying no changes in the melt depletion buoyancy and oceanic crustal thickness, and because the effect of higher temperatures on buoyancy would affect similarly the two reference continental and oceanic columns.

We have considered a homogeneous mantle potential temperature for the calibration of mantle densities in the reference case. However, mantle potential temperature is associated with significant uncertainty and may exhibit lateral variations below continents and could be lower or higher than the reference mantle potential temperature beneath mid-ocean ridges (Fullea et al., 2021). These variations correlate with the size and age of the continents, with the distance to hotspots and subduction zones, and with lithospheric thickness, related to differences in secular cooling, hotspot activity and mantle convection (e.g., Reston and Morgan, 2004; Jain et al., 2019; Munch et al., 2020; Fullea et al., 2021; Sternai, 2020). Shear wave anomalies also suggest a more heterogeneous sub-lithospheric mantle beneath continents than below the oceanic domain that appears to be linked to the most recent regional tectonic and/or magmatic event (Röhm et al., 2000; Schaeffer and Lebedev, 2013). Lévy and Jaupart (2011) suggest that the present day potential mantle temperature beneath stable continents far from hotspots is close to the one beneath mid-ocean ridges. A different mantle potential temperature beneath continents would change the temperature in the continental lithospheric mantle and in the sub-lithospheric mantle (upper-mantle 0 $-$600 km depth). A moderate difference of the temperature at the lithosphere-asthenosphere (< 100 K) boundary beneath stable continents far from hotspots would change the calibration of the average depletion buoyancy estimate of the continental lithospheric mantle by less than 10 kg/m^3. This potential temperature difference would only result in a deviation of continental elevation in the order of 100 $-$200 m. We note, however, that temperature in the mantle is linked to the density distribution and calibrated with geophysical observations (e.g., Fig. 7) that do not allow large variations in the sub-lithospheric mantle.

7.6. Anomalous hotspots cases

While we specifically focus on reference cases for the oceanic and continental domains that exclude anomalies such as those related to hotspots, we here briefly discuss the implication of anomalously high mantle temperature for ridge elevation. We compute the effect of higher mantle temperature on oceanic crust thickness, mantle depletion, and elevation using the setup of model M2 (Fig. S16). A higher mantle potential temperature results in higher depletion buoyancy of the oceanic lithospheric mantle, higher oceanic crust thickness, and consequently higher elevation of the mid-ocean ridge. Ridge elevation depends on the compensation depth and the bottom limit of the anomalous mantle temperature. Oceanic crustal thickness and mid-ocean ridge elevation increases linearly with degree of melting linked to increased mantle potential temperature or alternatively to lower mantle solidus related to mantle composition (e.g., Matthews et al., 2021; Dalton et al., 2014; Niu, 2017; Niu, 2021). Oceanic crustal thickness provides the main control on ridge elevation while increase of mantle depletion buoyancy contributes 30% of the elevation increase.

The Icelandic hotspot is one of the most prominent examples on Earth of the interaction between a mantle hotspot and a mid-ocean ridge. A temperature anomaly in the range of $+$ 45–80 K explains the variation of crustal thickness (8.5–12.5 km) and water depth (1600 to 800 m) of the Reykjanes ridge between the Bight fracture zone (57 °N) and the southern limit of the Greenland-Iceland-Faroes ridge (63 °N), assuming a depth extent of the thermal anomaly of about 200 km (e.g., (Schaeffer and Lebedev, 2013; French and Romanowicz, 2015)) and a mantle source that is the same as our reference case, ignoring along strike variations (e.g., Funck et al., 2017; Zha et al., 2022; Martinez et al., 2020). A moderate temperature anomaly of $+100$ K beneath Iceland is in the lower range of the most recent petrological-based estimate 160 ± 50 K (Matthews et al., 2021), in agreement with estimated

values from seismological data, and consistent with predictions from geodynamic modeling using a thermal anomaly 50 and 125 K (Vinnik et al., 2005; Ribe et al., 1995; Allen and Tromp, 2005). The observed average crustal thickness on Iceland (∼ 27.5 km) (e.g., Torsvik et al., 2015; Funck et al., 2017) combined with a mantle thermal anomaly of 100 K allows reproducing its mean elevation (∼ +800 m). The inferred thermal anomaly of 100 K, however, does not explain the observed crustal thickness of 27.5 km on Iceland which requires invoking either active mantle upwelling, a more fertile and/or more hydrated mantle source, or a pre-existing 10–15 km thick continental crust beneath the Greenland-Iceland-Faroes ridge (e.g., Torsvik et al., 2015; Foulger et al., 2020; Martinez et al., 2020).

7.7. Comparison with previous studies

Previous studies have attempted to evaluate controls on continent and ocean elevation (e.g., Lamb et al., 2020; Afonso et al., 2008; Fullea et al., 2021). The results from Fullea et al. (2021) include a 3-D density model of the Earth upper-mantle based on a joint inversion of surface-wave phase velocities, surface heat flow, elevation, and gravity that can be compared with our results. Their model includes a thermodynamic framework that solves for the mineral assemblage using the Gibbs free energy minimization approach for temperatures higher than 500 °C using 5 components CFMAS composition and database from Stixrude and Lithgow-Bertelloni (2011) similarly to our study. We use a 7 components NCFMASCr system and take into account the thermal structure beneath the MOR, associated MOR melting and source depletion. We show that Cr is important to better constrain the plagioclase and spinel fields which is not included in Fullea et al. (2021). We also show that properly including the MOR thermal structure and associated melt prediction is critical to properly estimate density variations in the reference MOR column (see also, Afonso et al., 2008), which is not included in Fullea et al. (2021). We note that the global tomography from Fullea et al. (2021) provides a good estimate of the depth of the lithosphere-asthenosphere boundary and gives interesting insights into lateral compositional variations in the mantle. In particular, their 3-D model shows that the sub-lithospheric mantle is heterogeneous but that resulting density variations are small $\pm 3-7$ kg/m^3 in agreement with our assumption to consider the reference sub-lithospheric mantle as homogeneous at first order.

7.8. Limitations

Our results are consistent with knowledge on density distribution of the shallow sub-lithospheric mantle, depletion buoyancy of the CLM, crustal densities, MOR and continent elevations. We summarize here the main limitations of the approach used in this study. We do not consider hydrothermal circulation that may modify cooling of the oceanic lithosphere (e.g., Crameri et al., 2019; Li et al., 2017; Grose and Afonso, 2013). The resulting effect on MOR elevation is small in the order of 100 m (Grose and Afonso, 2013). We use constant bulk thermal properties for the crust and the mantle. Variable thermal properties would change the temperature distribution with depth and consequently change the calibrated densities. However, this does not affect the main conclusions of the work presented here. Our models do not include self-consistent two-phase flow modelling of melt extraction and migration that would likely result in a different density distribution beneath the MOR (e.g., Behn and Grove, 2015; Crameri et al., 2019). This may change the actual calibrated densities but we anticipate that this would only result in a small change of the elevation difference between MOR and stable continents. Our geodynamic model M1 uses only one mantle composition and associated thermodynamic solution resulting in an underestimate of the density increase with oceanic lithosphere cooling away from the ridge. This has a minor impact on the prediction of the density distribution and water depth of the mid-ocean ridge and results in a too slow thermal subsidence with age. A more accurate modelling approach would require efficient real time thermodynamic computation during particle advection.

8. Conclusion

Here we provide a new analysis of the elevation of stable continental areas and mid-ocean ridges. We use 1-D and 2-D models that include petrologic thermodynamically consistent density distribution within the continental lithospheric mantle and beneath the mid-ocean ridges to predict the relative elevation between these domains. The resulting densities for the crust, continental mantle lithosphere, sub-lithospheric mantle, and for the mid-ocean ridge column are calibrated against the observed elevation difference. Models using the thermodynamic consistent densities allow calibrating simple 1-D and 2-D models that include densities that only depend on temperature based on the classic Boussinesq approximation (e.g., Fig. 13). Both the complex pressure, temperature, and composition based densities, and the simple calibrated densities that depend on temperature only allow accurate prediction of topography in geodynamic modelling. We reach the following specific conclusions:

1. Stable continents far from hotspots with a crustal thickness of 35 ± 5 km have an elevation of $+400 \pm 400$ m. Active mid-ocean ridges far from hotspots have an elevation of about -2750 ± 250 m on average. The reference relative elevation between continents and mid-ocean ridges is consequently about 3150 m with a characteristic water depth at the ridge of 2750 m.
2. Thermodynamic modelling reveals that mantle composition SP2008 (Mg#89, high Al_2O_3, high Na_2O) from Simon and Podladchikov (2008) provides a good reference fertile mantle composition as it reproduces the shallow upper-mantle density profile of the sub-lithospheric mantle consistent with geophysical data.
3. Using a set of characteristic mantle compositions based on xenolith studies, thermodynamic calculations provide an approximation of the depletion buoyancy of the lithospheric mantle for Phanerozoic lithosphere $\Delta\rho_X \sim 10-20$ kg/m^3, for Proterozoic lithosphere $\Delta\rho_X \sim 30-35$ kg/m^3 while it is larger than 40 kg/m^3 for Archean lithospheres.
4. 2-D geodynamic models, that include mantle melting and densities from thermodynamic calculations and 1-D isostatic calculations show that the relative elevation difference between mid-ocean ridges and continents depends on crustal density, mantle composition and density distribution, and degree of depletion of the lithospheric mantle.
5. We calibrate average continental crustal density and depletion buoyancy based on the thermodynamic consistent approach to establish the reference densities that can be used for continental mantle lithosphere and sub-lithospheric mantle in models that follow the classic Boussinesq approximation where density depends on thermal expansivity. The calibrated reference density of the sub-lithospheric mantle is ~ 3310 kg/m^3 at 0°C in our thermo-mechanical models based on the Boussinesq approximation. The average crustal density $\overline{\rho}_c$ and average continental mantle lithosphere depletion buoyancy $\overline{\Delta\rho}_{X,CLM}$ that fit the observed elevation difference between reference stable Phanerozoic continental lithosphere at +400 m elevation and active mid-ocean ridge at 2750 m water depth far from hotspots follow this relation:

$$\overline{\rho}_c = -2.5\overline{\Delta\rho}_{X,CLM} + 2783$$

with preferred values being $\overline{\rho}_c = 2833$ kg/m^3 and $\overline{\Delta\rho}_{X,CLM} = -20$ kg/m^3 consistent with geophysical and thermodynamic constraints.
6. The calibrated average depletion buoyancy of the continental lithospheric mantle varies between -20 and -50 ± 15 kg/m^3 for varying lithospheric thickness between 125 and 280 km consistent with estimates using thermodynamic calculations.

We finally provide a collection of Jupyter notebooks and the databases including geographic data and grids of the thermodynamic calculations for all mantle compositions presented as supplementary material that allow readers to reproduce the work done in this study and/ or to calibrate models with their particular preferences.

Author contributions

T.T. contributed the numerical models and analysed the global data. R.H. assisted with the 2-D modelling and contributed ideas on mid-ocean ridge spreading. G.L participated with developing the 2-D geodynamics code and with parameterizing model setup. N.R. provided his expertise in thermodynamics and did the thermodynamics calculations. All authors contributed to developing the concepts and to writing the manuscript.

Declaration of Competing Interest

The authors declare that they have no known competing financial interests or personal relationships that could have appeared to influence the work reported in this paper.

Data availability

Data is available through FigShare and Github. Weblink is given in the supplementary material.

Acknowledgments

This study is funded through the COLORS project by TOTALENERGIES and The Research council of Norway. We thank Uninett Sigma2 for computing time of project NN4704K. We are grateful to B. Steinberger, C. Kreemer and N. Shapiro for sharing their dataset. We thank F. Despinois, T. Cornu and C. Gout for stimulating discussions and providing support for this work. We thank Oyvind Natvik and IT department of the University of Bergen for computational resources and help. We thank the editor Gillian Foulger and the two reviewers Javier Fullea and Yaoling Niu for their thoughtful and constructive reviews that helped improve the manuscript. Supplementary material that includes videos, the entire dataset and Jupyter notebooks to reproduce and to display results presented in this study are accessible through github and figshare repositories.

Appendix A. Thermo-mechanical model

A.1. Method

This study uses the modified 2-D Arbitrary-Lagrangian–Eulerian (ALE) thermo-mechanically coupled finite element code FANTOM (Thieulot, 2011; Theunissen and Huismans, 2019), coupled to melt prediction and density prediction from thermodynamic calculations, to calibrate the density structure beneath continents and mid-ocean ridges. The model computes momentum and mass conservation of plane-strain incompressible fluids to solve for Stokes flow:

$$\nabla\cdot\left(\mu_{eff}\left(\nabla\mathbf{v}+(\nabla\mathbf{v})^{T}\right)\right)-\nabla P+\rho\boldsymbol{g}=0 \tag{A.1}$$

where P is the pressure, $\mathbf{v}$ is the velocity, μ_{eff} the effective viscosity, ρ the density and g the gravity acceleration. This is coupled with time (t)-dependent heat conservation following:

$$\frac{\partial T}{\partial t}=\frac{\nabla\cdot(k\nabla T)}{\rho c_p}-v\nabla T+\frac{H}{\rho c_p}+\frac{v_z\alpha_T g T}{c_p}-\frac{T\Delta S}{c_p}\frac{\partial\phi}{\partial t} \tag{A.2}$$

where T is the temperature, c_p the specific heat capacity, α thermal expansion, H the radiogenic heat production and the fourth term in the right-hand side being the temperature correction for adiabatic heating and cooling when material moves vertically at velocity v_z. The final term in the heat balance equation expresses the absorption of latent heat related to the phase change from solid to melt where ΔS is the change of entropy on melting, $\partial\phi/\partial t$ is the time derivative of the melt fraction, ϕ. The coupling is done through nonlinear temperature (T)- and pressure (P)-dependent rheologies, as well as the temperature dependence of buoyancy using the extended Boussinesq approximation (Christensen and Yuen, 1985; Gerya, 2010), which considers that changes in density (ρ) are small enough to approximate the conservation of mass by an incompressible flow:

$$\nabla\cdot\mathbf{v}=0 \tag{A.3}$$

A.2. Rheology

When stress is below frictional-plastic yield, the flow is viscous and is specified by temperature-dependent nonlinear power law rheologies based on laboratory measurements on ‘wet’ quartz (Gleason and Tullis, 1995), on dry Maryland diabase (Mackwell et al., 1998), and olivine (Karato and Wu, 1993). The effective viscosity, μ_{eff}, in the power law rheology is of general form:

$$\mu_{eff}=fA^{-1/n}\dot{E}_2^{(1-n)/2n}exp\left(\frac{Q+VP}{nRT}\right) \tag{A.4}$$

where $\dot{E}_2$is the second invariant of the deviatoric strain rate tensor $\frac{1}{2}\dot{\varepsilon}_{ij}\dot{\varepsilon}_{ij}$, n is the power-law exponent, A is the pre-exponential scaling factor, Q is the activation energy, V is the activation volume, P is the pressure, T is the absolute temperature and R is the universal gas constant. A, n, Q and V are derived from laboratory experiments and the parameter values are listed in Table 3. The factor f is used to scale viscosities calculated from the reference quartz, diabase and olivine flow laws. This scaling produces strong and weak crust and reproduces the difference between ‘wet’ and ‘dry’ olivine. Frictional-plastic (Mohr–Coulomb) yielding occurs when:

$$\sigma_y = \sqrt{J_2} = Ccos(\phi_{eff}) + Psin(\phi_{eff}) \tag{A.5}$$

where $J_2$is the second invariant of the deviatoric stress, C is the cohesion and ϕ_{eff} is the effective internal angle of friction following $Psin(\phi_{eff}) = (P - P_f)\sin(\phi)$, where P_f is the pore fluid pressure. This approximates frictional sliding in rocks, including pore-fluid pressure effects. This yield criterion is equivalent to Drucker-Prager in 2-D plane strain approximation (Wojciechowski, 2018).

The model accounts for frictional-plastic strain softening, which is responsible for strain localization in the brittle layer, and is introduced by a linear decrease of $\phi_{eff}(\varepsilon)$ from 15° to 2° and $C_{eff}(\varepsilon)$ from 20 to 4 MPa with respect to plastic strain (ε) between ε_0 and ε_0 (Buck, 1993; Huismans and Beaumont, 2002; Lavier et al., 1999; Lavier et al., 2000). $\phi_{eff}(\varepsilon_0) \approx 15°$ corresponds to hydrostatic pore pressure (Huismans and Beaumont, 2002). In our model ε_0 and ε_1 are set to 5% and 105% respectively (Fig. S13). For mantle rocks, we use $\phi_{eff}(\varepsilon_1) = 4°$ and the cohesion is kept constant with $C_{eff}(\varepsilon_1) = 20$MPa (Theunissen and Huismans, 2022). The sub-lithospheric mantle is fully plastically weakened when exhumed inhibiting strain localization and ensuring a symmetric spreading and a smooth relief at the sea-floor.

Appendix B. Melt prediction using linearized mantle solidus

The procedure used for the melt prediction is based on Scott (1992); Nielsen and Hopper, 2004; Simon et al., 2009; Lu and Huismans, 2021. The temperature of melting is constrained to lie on the solidus:

$$T_s = T_{s0} + \left.\frac{\partial T}{\partial z}\right|_X z + \left.\frac{\partial T_s}{\partial X}\right|_z \left(X - 1\right) \tag{B.1}$$

where T_s is the current solidus temperature, T_{s0} is the solidus temperature at the surface, $\partial T/\partial z|_X$ is the gradient of the solidus temperature with depth, and $\partial T_s/\partial X|_z$ is the change in solidus temperature with depletion.

The depth derivative of the solidus, $\partial T/\partial z|_X$ is a linear approximation based on the parametrization of (McKenzie and Bickle, 1988). This linear approximation is justified since the solidus is almost linear up to pressures of approximately 4 GPa (120 km depth) and it is unlikely significant amounts of melting occur below these depths in a rifting/mid-ocean ridge environment.

We define a wet solidus which corresponds to a reduction of the dry solidus by 200°C. Inside the damp melting domain between the wet and dry solidus, melt fractions are parametrized to be 0 on the wet solidus and 0.02 on the dry solidus (Choblet and Parmentier, 2001).

The $\partial T_s/\partial X|_z(X-1)$ term of Eq. B.1 takes into account the change to the solidus temperature that occurs as a result of compositional depletion of the mantle upon melting. As the depletion factor X progressively increases from its initial starting value of 1, the mantle becomes more difficult to melt, and the solidus temperature increases accordingly. Following Nielsen and Hopper (2004) the changing incremental melt fraction may be calculated using $d\phi = (T - T_s)/(L + \partial T_s/\partial\phi)$, where $\partial T_s/\partial\phi = (X/(1-\phi))\partial T_s/\partial X$ and $L = T\Delta S/c_p$. At each time step in the model evolution, the solidus temperature is updated, and incremental melt fractions are computed using the expression for $d\phi$.

Appendix C. Melt prediction using thermodynamic calculations

In model M1, melt prediction is based on thermodynamic calculation using the characteristic fertile mantle composition SP2008 from Simon and Podladchikov (2008) (Fig. 7) The melting solution for dry conditions is calculated at equilibrium meaning that there is a mix of melt and solid in a closed system (batch melting). As a consequence it is theoretically not possible to directly use this solution to determine the melt fraction and the density distribution inside the melt window. Indeed, in nature melt rapidly separates from the solid residuum resulting in efficient melt extraction from the mantle (Spiegelman, 1993; Kelemen et al., 1997). Although about 15% melting is expected in most calculations due to decompression alone, geophysical methods detect less than 2% of retained melt (Team, 1998; Evans et al., 1999; Goes et al., 2012; Eilon and Abers, 2017). The rest is extracted quickly, so that the actual melt content is much smaller than the total degree of melting. Also thermodynamic models and laboratory experiments show that fractionation (incremental batch melting) results in lower productivity than batch melting experiments (Hirschmann et al., 1998) (Fig. S10). We use only one thermodynamic solution assuming a linear relationship between total melt fraction from batch melting and incremental batch melting. Calibration of this parameter to fit the predicted 6.5 km thick oceanic crust provides a value of $\phi/\phi_{batch} = 0.55$ consistent with earlier modeling (e.g., Hirschmann et al. (1998)) (Fig. S10). In model M1, material produces additional melt only if the predicted melt fraction ϕ is higher than the highest melt fraction encountered during its history.

Appendix D. Coupling and feedback between melt production and thermo-mechanical solution

Melt prediction routines are coupled to the thermo-mechanical model through the use of the lithostatic pressure (model M1) or depth (model M2) and temperature. The model accounts for feedback from melting on temperature, viscosity and density. Note that feedback relations on density are presented in the main text.

D.1. Pressure

The linearized melt production routine in model type M2 uses a temperature-depth dependent linear relationships to define solidus. To avoid local variations related to fault related topography, we use a smoothed version of the free surface as a reference to compute the depth. For consistency with the linearized melt production routine where the solidus is defined with the depth, we use the lithostatic pressure to read tables from the thermodynamic solutions in model M1. Based on model outputs the relative continent/ocean overpressure (difference between dynamic pressure and lithostatic pressure) in the mantle is small between 1 and 5 MPa on average that represents an elevation difference between 30 and 150 m (Fig. S11). Note that water load is included in the lithostatic pressure in our model.

D.2. Feedback on temperature

Feedback on temperature is expressed in the final term of the heat balance Eq. A.2. This represents the absorption of latent heat related to the phase change from solid to melt which depends on the change of entropy of melting and the melt production rate with time.

D.3. Feedback on viscosity

Feedback on mantle viscosity is introduced to consider the effect of melt weakening and dehydration strengthening. It is generally accepted that less than 5% of melt is enough to extract all water from a hydrous mantle (Hirth and Kohlstedt, 1996; Asimow et al., 2004). Following previous studies (e.g., Braun et al., 2000; Choblet and Parmentier, 2001; Nielsen and Hopper, 2004; Simon et al., 2009), we model the effect of dehydration strengthening in the damp melting regime by use of a simple linear parametrization. We employ a linear scaling factor to increase effective viscosity over a range of $\Omega = 1 - 5$ for melt fractions between 0 and 2 percent. For melt fractions greater than 2 percent, we set Ω to 5, reflecting the full increase in viscosity above the dry solidus owing to dehydration strengthening. 1% of melt retention introduces a viscosity reduction of about 1.2, i.e. $\mu/\mu_0 = exp(-a\phi)$ where a is a constant between 30 and 45 (e.g., Nielsen and Hopper, 2004 and references therein). The effect of melt weakening on viscosity is then countered by dehydration strengthening (e.g., Karato, 1986; Hirth and Kohlstedt, 1996). Finally feedback from melting on effective viscosity (Eq. A.4) express as following:

$$\mu = \mu_{eff}\Omega exp(-a\phi) \tag{D.1}$$

The net effect results in mantle strengthening with a factor of about 4 on viscosities after the mantle went through wet and dry melting windows (e.g., Nielsen and Hopper, 2004, and references therein).

Appendix E. Supplementary data

Supplementary data associated with this article can be found, in the online version, at https://doi.org/10.1016/j.earscirev.2022.104153.

References

Abbott, D., Burgess, L., Longhi, J., Smith, W.H.F., 1994. An empirical thermal history of the earth's upper mantle. J. Geophys. Res.: Solid Earth 99, 13835–13850. https://doi.org/10.1029/94JB00112.

Afonso, J.C., Fernàndez, M., Ranalli, G., Griffin, W.L., Connolly, J.A.D., 2008. Integrated geophysical-petrological modeling of the lithosphere and sublithospheric upper mantle: methodology and applications. Geochem. Geophys. Geosyst. 9 https://doi.org/10.1029/2007GC001834.

Afonso, J.C., Salajegheh, F., Szwillus, W., Ebbing, J., Gaina, C., 2019. A global reference model of the lithosphere and upper mantle from joint inversion and analysis of multiple data sets. Geophys. J. Int. 217, 1602–1628. https://doi.org/10.1093/gji/ggz094.

Afonso, J.C., Schutt, D.L., 2012. The effects of polybaric partial melting on density and seismic velocities of mantle restites. Lithos 134-135, 289–303. https://doi.org/10.1016/j.lithos.2012.01.009.

Airy, G.B., 1855. III. On the computation of the effect of the attraction of mountain-masses, as disturbing the apparent astronomical latitude of stations in geodetic surveys. Phil. Trans. R. Soc. 145, 101–104. https://doi.org/10.1098/rstl.1855.0003.

Allen, J., Beaumont, C., 2016. Continental margin syn-rift salt tectonics at intermediate width margins. Basin Res. 28, 598–633. https://doi.org/10.1111/bre.12123.

Allen, R.M., Tromp, J., 2005. Resolution of regional seismic models: squeezing the Iceland anomaly. Geophys. J. Int. 161, 373–386. https://doi.org/10.1111/j.1365-246X.2005.02600.x.

Amante, C., Eakins, B., 2009. Etopo1 1 arc-minute global relief model: procedures, data sources and analysis. NOAA Technical Memorandum NESDIS NGDC 24. https://doi.org/10.7289/V5C8276M.

Anderson, D.L., 2007. New Theory of the Earth, second ed. Cambridge University Press. https://doi.org/10.1017/CBO9781139167291.

Andrés-Martínez, M., Pérez-Gussinyé, M., Armitage, J., Morgan, J.P., 2019. Thermomechanical implications of sediment transport for the architecture and evolution of continental rifts and margins. Tectonics 38, 641–665. https://doi.org/10.1029/2018TC005346.

Artemieva, I.M., 2006. Global 1x1 thermal model tc1 for the continental lithosphere: implications for lithosphere secular evolution. Tectonophysics 416, 245–277. https://doi.org/10.1016/j.tecto.2005.11.022.

Artemieva, I.M., 2009. The continental lithosphere: reconciling thermal, seismic, and petrologic data. Lithos 109, 23–46. https://doi.org/10.1016/j.lithos.2008.09.015.

Artemieva, I.M., 2019. Lithosphere structure in europe from thermal isostasy. Earth-Sci. Rev. 188, 454–468. https://doi.org/10.1016/j.earscirev.2018.11.004.

Asimow, P.D., Dixon, J.E., Langmuir, C.H., 2004. A hydrous melting and fractionation model for mid-ocean ridge basalts: Application to the mid-atlantic ridge near the azores. Geochem. Geophys. Geosyst. 5 https://doi.org/10.1029/2003GC000568.

Asimow, P.D., Hirschmann, M.M., Stolper, E.M., 2001. Calculation of Peridotite Partial Melting from Thermodynamic Models of Minerals and Melts, IV. Adiabatic Decompression and the Composition and Mean Properties of Mid-ocean Ridge Basalts. J. Petrol. 42, 963–998. https://doi.org/10.1093/petrology/42.5.963.

Behn, M.D., Grove, T.L., 2015. Melting systematics in mid-ocean ridge basalts: application of a plagioclase-spinel melting model to global variations in major element chemistry and crustal thickness. J. Geophys. Res.: Solid Earth 120, 4863–4886. https://doi.org/10.1002/2015JB011885.

Bishop, P., 2007. Long-term landscape evolution: linking tectonics and surface processes. Earth Surf. Proc. Land. 32, 329–365. https://doi.org/10.1002/esp.1493.

Braun, J., 2010. The many surface expressions of mantle dynamics. Nat. Geosci. 3, 825–833. https://doi.org/10.1038/ngeo1020.

Braun, J., Deschamps, F., Rouby, D., Dauteuil, O., 2013. Flexure of the lithosphere and the geodynamical evolution of non-cylindrical rifted passive margins: Results from a numerical model incorporating variable elastic thickness, surface processes and 3d thermal subsidence. Tectonophysics 604, 72–82. https://doi.org/10.1016/j.tecto.2012.09.033 progress in understanding the South Atlantic margins.

Braun, M.G., Hirth, G., Parmentier, E., 2000. The effects of deep damp melting on mantle flow and melt generation beneath mid-ocean ridges. Earth Planet. Sci. Lett. 176, 339–356. https://doi.org/10.1016/S0012-821X(00)00015-7.

Brune, S., Heine, C., Perez-Gussinye, M., Sobolev, S.V., 2014. Rift migration explains continental margin asymmetry and crustal hyper-extension. Nat. Commun. 5 https://doi.org/10.1038/ncomms5014.

Buck, W.R., 1993. Effect of lithospheric thickness on the formation of high- and low-angle normal faults. Geology 21, 933–936. https://doi.org/10.1130/0091-7613(1993)021<0933:EOLTOT>2.3.CO;2.

Burov, E., Poliakov, A., 2003. Erosional forcing on basin dynamics : new aspects of syn- and post-rift evolution. In: niewland, d.a. (Ed.), New insights in structural interpretation and modelling, vol. 212. Special Publication - Geological Society of London, pp. 209–224.

Cammarano, F., Guerri, M., 2017. Global thermal models of the lithosphere. Geophys. J. Int. 210, 56–72. https://doi.org/10.1093/gji/ggx144.

Carlson, R.L., Raskin, G.S., 1984. Density of the ocean crust. Nature 311, 555–558. https://doi.org/10.1038/311555a0.

Celli, N.L., Lebedev, S., Schaeffer, A.J., Ravenna, M., Gaina, C., 2020. The upper mantle beneath the South Atlantic Ocean, South America and Africa from waveform tomography with massive data sets. Geophys. J. Int. 221, 178–204. https://doi.org/10.1093/gji/ggz574.

Chatterjee, N.D., Leistner, H., Terhart, L., Abraham, K., Klaska, R., 1982. Thermodynamic mixing properties of corundum–eskolaite, α–(Al, Cr+3)2O3, crystalline solutions at high temperatures and pressures. Am. Mineral. 67, 725–735. https://pubs.geoscienceworld.org/msa/ammin/article/67/7-8/725/41412/Thermodynamic-mixing-properties-of-corundum.

Choblet, G., Parmentier, E., 2001. Mantle upwelling and melting beneath slow spreading centers: effects of variable rheology and melt productivity. Earth Planet. Sci. Lett. 184, 589–604. https://doi.org/10.1016/S0012-821X.

Christensen, N., Mooney, W., 1995. Seismic velocity structure and composition of the continental crust - a global view. J. Geophys. Res.-Solid Earth 100, 9761–9788. https://doi.org/10.1029/95JB00259.

Christensen, U.R., Yuen, D.A., 1985. Layered convection induced by phase transitions. J. Geophys. Res.: Solid Earth 90, 10291–10300. https://doi.org/10.1029/JB090iB12p10291.

Christeson, G.L., Goff, J.A., Reece, R.S., 2019. Synthesis of oceanic crustal structure from two-dimensional seismic profiles. Rev. Geophys. 57, 504–529. https://doi.org/10.1029/2019RG000641.

Coblentz, D.D., Richardson, R.M., Sandiford, M., 1994. On the gravitational potential of the earth's lithosphere. Tectonics 13, 929–945. https://doi.org/10.1029/94TC01033.

Courtillot, V., Davaille, A., Besse, J., Stock, J., 2003. Three distinct types of hotspots in the earth's mantle. Earth Planet. Sci. Lett. 205, 295–308. https://doi.org/10.1016/S0012-821X(02)01048-8.

Crameri, F., Conrad, C.P., Montési, L., Lithgow-Bertelloni, C.R., 2019. The dynamic life of an oceanic plate. Tectonophysics 760, 107–135. https://doi.org/10.1016/j.tecto.2018.03.016.

Crosby, A.G., Fishwick, S., White, N., 2010. Structure and evolution of the intracratonic congo basin. Geochem. Geophys. Geosyst. 11 https://doi.org/10.1029/2009GC003014.

Crosby, A.G., White, N.J., Edwards, G.R.H., Thompson, M., Corfield, R., Mackay, L., 2011. Evolution of deep-water rifted margins: testing depth-dependent extensional models. Tectonics 30. https://doi.org/10.1029/2010TC002687.

Dalton, C.A., Langmuir, C.H., Gale, A., 2014. Geophysical and geochemical evidence for deep temperature variations beneath mid-ocean ridges. Science 344, 80–83. https://doi.org/10.1126/science.1249466.

Davies, D.R., Valentine, A.P., Kramer, S.C., Rawlinson, N., Hoggard, M.J., Eakin, C.M., Wilson, C.R., 2019. Earth's multi-scale topographic response to global mantle flow. Nat. Geosci. 12, 845–850. https://doi.org/10.1038/s41561-019-0441-4.

Davis, F.A., Tangeman, J.A., Tenner, T.J., Hirschmann, M.M., 2009. The composition of KLB-1 peridotite. Am. Mineral. 94, 176–180. https://doi.org/10.2138/am.2009.2984.

Duretz, T., Asti, R., Lagabrielle, Y., Brun, J.P., Jourdon, A., Clerc, C., Corre, B., 2020. Numerical modelling of cretaceous pyrenean rifting: the interaction between mantle exhumation and syn-rift salt tectonics. Basin Res. 32, 652–667. https://doi.org/10.1111/bre.12389.

Duretz, T., Petri, B., Mohn, G., Schmalholz, S.M., Schenker, F.L., Müntener, O., 2016. The importance of structural softening for the evolution and architecture of passive margins. Nat. - Sci. Rep. 6, 38704. https://doi.org/10.1038/srep38704.

Dziewonski, A.M., Anderson, D.L., 1981. Preliminary reference earth model. Physics of the Earth and Planetary Interiors 25, 297–356. https://doi.org/10.1016/0031-9201(81)90046-7.

Eilon, Z.C., Abers, G.A., 2017. High seismic attenuation at a mid-ocean ridge reveals the distribution of deep melt. Sci. Adv. 3 https://doi.org/10.1126/sciadv.1602829.

Evans, R.L., Tarits, P., Chave, A.D., White, A., Heinson, G., Filloux, J.H., Toh, H., Seama, N., Utada, H., Booker, J.R., Unsworth, M.J., 1999. Asymmetric electrical structure in the mantle beneath the east pacific rise at 17s. Science 286, 752–756. https://doi.org/10.1126/science.286.5440.752.

Flament, N., 2019. The deep roots of earth's surface. Nat. Geosci. 12, 787–788. https://doi.org/10.1038/s41561-019-0447-y.

Forsyth, D.W., 1992. Finite extension and low-angle normal faulting. Geology 20, 27–30. https://doi.org/10.1130/0091-7613(1992)020<0027:FEALAN>2.3.CO;2.

Forte, A.M., Perry, H.K.C., 2000. Geodynamic evidence for a chemically depleted continental tectosphere. Science 290, 1940–1944. https://doi.org/10.1126/science.290.5498.1940.

Foulger, G.R., Doré, T., Emeleus, C.H., Franke, D., Geoffroy, L., Gernigon, L., Hey, R., Holdsworth, R.E., Hole, M., Höskuldsson, Á., Julian, B., Kusznir, N., Martinez, F., McCaffrey, K.J., Natland, J.H., Peace, A.L., Petersen, K., Schiffer, C., Stephenson, R., Stoker, M., 2020. The iceland microcontinent and a continental greenland-iceland-faroe ridge. Earth-Sci. Rev. 206, 102926. https://doi.org/10.1016/j.earscirev.2019.102926.

French, S.W., Romanowicz, B., 2015. Broad plumes rooted at the base of the earth's mantle beneath major hotspots. Nature 525, 95–99. https://doi.org/10.1038/nature14876.

French, S.W., Romanowicz, B.A., 2014. Whole-mantle radially anisotropic shear velocity structure from spectral-element waveform tomography. Geophys. J. Int. 199, 1303–1327. https://doi.org/10.1093/gji/ggu334.

Fullea, J., Lebedev, S., Martinec, Z., Celli, N.L., 2021. WINTERC-G: mapping the upper mantle thermochemical heterogeneity from coupled geophysical–petrological inversion of seismic waveforms, heat flow, surface elevation and gravity satellite data. Geophys. J. Int. 226, 146–191. https://doi.org/10.1093/gji/ggab094.

Funck, T., Geissler, W.H., Kimbell, G.S., Gradmann, S., Erlendsson, Ö., McDermott, K., Petersen, U.K., 2017. Moho and basement depth in the ne atlantic ocean based on seismic refraction data and receiver functions. Geol. Soc., London, Spec. Publ. 447, 207–231. https://doi.org/10.1144/SP447.1.

Gaul, O.F., Griffin, W., O'Reilly, S.Y., Pearson, N., 2000. Mapping olivine composition in the lithospheric mantle. Earth Planet. Sci. Lett. 182, 223–235. https://doi.org/10.1016/S0012-821X(00)00243-0.

Gerya, T., 2010. Numerical Geodynamic Modelling. Cambridge University Press.

Gleason, G.C., Tullis, J., 1995. A flow law for dislocation creep of quartz aggregates determined with the molten salt cell. Tectonophysics 247, 1–23. https://doi.org/10.1016/0040-1951(95)00011-B, 30 Years of Tectonophysics a Special Volume in Honour of Gerhard Oertel.

Globig, J., Fernandez, M., Torne, M., Verges, J., Robert, A., Faccenna, C., 2016. New insights into the crust and lithospheric mantle structure of Africa from elevation, geoid, and thermal analysis. J. Geophys. Res.-Solid Earth 121, 5389–5424. https://doi.org/10.1002/2016JB012972.

Goes, S., Armitage, J., Harmon, N., Smith, H., Huismans, R., 2012. Low seismic velocities below mid-ocean ridges: Attenuation versus melt retention. Journal of Geophysical Research: Solid. Earth 117. https://doi.org/10.1029/2012JB009637.

Goteti, R., Ings, S.J., Beaumont, C., 2012. Development of salt minibasins initiated by sedimentary topographic relief. Earth Planet. Sci. Lett. 339, 103–116. https://doi.org/10.1016/j.epsl.2012.04.045.

Griffin, W.L., O'Reilly, S.Y., Ryan, C.G., 1999. The composition and origin of sub-continental lithospheric mantle. Geochem. Soc. Spec. Publ., Houston, TX 6, 13–45. https://doi.org/10.7312/karn12738-005.

Griffin, W.L., O'Reilly, S.Y., Afonso, J.C., Begg, G.C., 2008. The composition and evolution of lithospheric mantle: a re-evaluation and its tectonic implications. J. Petrol. 50, 1185–1204. https://doi.org/10.1093/petrology/egn033.

Grose, C.J., Afonso, J.C., 2013. Comprehensive plate models for the thermal evolution of oceanic lithosphere. Geochem. Geophys. Geosyst. 14, 3751–3778. https://doi.org/10.1002/ggge.20232.

Guerri, M., Cammarano, F., Tackley, P., 2016. Modelling earth's surface topography: decomposition of the static and dynamic components. Phys. Earth Planet. Inter. 261, 172–186. https://doi.org/10.1016/j.pepi.2016.10.009.

Gvirtzman, Z., Faccenna, C., Becker, T.W., 2016. Isostasy, flexure, and dynamic topography. Tectonophysics 683, 255–271. https://doi.org/10.1016/j.tecto.2016.05.041.

Hacker, B.R., Kelemen, P.B., Behn, M.D., 2015. Continental lower crust. In: Jeanloz, R., Freeman, K. (Eds.), Annual Review of Earth Planetary Sciences, VOL. 43. ANNUAL REVIEWS, 4139 EL CAMINO WAY, PO BOX 10139, PALO ALTO, CA 94303–0897 USA. volume 43 of Annual Review of Earth and Planetary Sciences, pp. 167+. doi: 10.1146/annurev-earth-050212-124117.

Hasterok, D., Chapman, D.S., 2007. Continental thermal isostasy: 2. Application to North America. J. Geophys. Res.: Solid Earth 112. https://doi.org/10.1029/2006JB004664.

Heiskanen, W.A., Moritz, H., 1967. Physical Geodesy. 1993 reprint ed. W.H. Freeman, San Francisco.

Herzberg, C., Asimow, P.D., Arndt, N., Niu, Y., Lesher, C.M., Fitton, J.G., Cheadle, M.J., Saunders, A.D., 2007. Temperatures in ambient mantle and plumes: Constraints from basalts, picrites, and komatiites. Geochem. Geophys. Geosyst. 8 https://doi.org/10.1029/2006GC001390.

Hirschmann, M.M., Ghiorso, M.S., Wasylenki, L.E., Asimow, P.D., Stolper, E.M., 1998. Calculation of Peridotite Partial Melting from Thermodynamic Models of Minerals and Melts. I. Review of Methods and Comparison with Experiments. J. Petrol. 39, 1091–1115. https://doi.org/10.1093/petroj/39.6.1091.

Hirth, G., Kohlstedt, D.L., 1996. Water in the oceanic upper mantle: implications for rheology, melt extraction and the evolution of the lithosphere. Earth Planet. Sci. Lett. 144, 93–108. https://doi.org/10.1016/0012-821X(96)00154-9.

Hoggard, M.J., Winterbourne, J., Czarnota, K., White, N., 2017. Oceanic residual depth measurements, the plate cooling model, and global dynamic topography. J. Geophys. Res.: Solid Earth 122, 2328–2372. https://doi.org/10.1002/2016JB013457.

Holland, T.J., Hudson, N.F., Powell, R., Harte, B., 2013. New Thermodynamic Models and Calculated Phase Equilibria in NCFMAS for Basic and Ultrabasic Compositions through the Transition Zone into the Uppermost Lower Mantle. J. Petrol. 54, 1901–1920. https://doi.org/10.1093/petrology/egt035.

Holland, T.J.B., Powell, R., 2011. An improved and extended internally consistent thermodynamic dataset for phases of petrological interest, involving a new equation of state for solids. J. Metamorph. Geol. 29, 333–383. https://doi.org/10.1111/j.1525-1314.2010.00923.x.

Huismans, R.S., Beaumont, C., 2002. Asymmetric lithospheric extension: The role of frictional plastic strain softening inferred from numerical experiments. Geology 30, 211–214. https://doi.org/10.1130/0091-7613(2002)030<0211:ALETRO>2.0.CO;2.

Huismans, R.S., Beaumont, C., 2003. Symmetric and asymmetric lithospheric extension: Relative effects of frictional-plastic and viscous strain softening. J. Geophys. Res.: Solid Earth 108. https://doi.org/10.1029/2002JB002026.

Huismans, R.S., Beaumont, C., 2008. Complex rifted continental margins explained by dynamical models of depth-dependent lithospheric extension. Geology 36, 163. https://doi.org/10.1130/G24231A.1.

Huismans, R.S., Beaumont, C., 2011. Depth-dependent extension, two-stage breakup and cratonic underplating at rifted margins. Nature 473, 74–U85. https://doi.org/10.1038/nature09988.

Ito, T., Simons, M., 2011. Probing asthenospheric density, temperature, and elastic moduli below the western united states. Science 332, 947–951. https://doi.org/10.1126/science.1202584.

Jagoutz, E., Palme, H., Baddenhausen, H., Blum, K., Cendales, M., Dreibus, G., Spettel, B., Lorenz, V., Wanke, H., 1979. The abundances of major, minor and trace elements in the earth's mantle as derived from primitive ultramafic nodules.

Jain, C., Rozel, A.B., Tackley, P.J., 2019. Quantifying the correlation between mobile continents and elevated temperatures in the subcontinental mantle. Geochem. Geophys. Geosyst. 20, 1358–1386. https://doi.org/10.1029/2018GC007586.

Jaupart, C., Mareschal, J.C., Iarotsky, L., 2016. Radiogenic heat production in the continental crust. Lithos 262, 398–427. https://doi.org/10.1016/j.lithos.2016.07.017.

Jennings, E.S., Holland, T.J.B., 2015. A Simple Thermodynamic Model for Melting of Peridotite in the System NCFMASOCr. J. Petrol. 56, 869–892. https://doi.org/10.1093/petrology/egv020.

Jennings, E.S., Holland, T.J.B., Shorttle, O., Maclennan, J., Gibson, S.A., 2016. The Composition of Melts from a Heterogeneous Mantle and the Origin of Ferropicrite: Application of a Thermodynamic Model. J. Petrol. 57, 2289–2310. https://doi.org/10.1093/petrology/egw065.

Jordan, T.H., 1979. Mineralogies, Densities and Seismic Velocities of Garnet Lherzolites and their Geophysical Implications. American Geophysical Union (AGU), pp. 1–14. https://doi.org/10.1029/SP016p0001.

Karabulut, H., Paul, A., Özbakır, A.D., Ergün, T., Şentürk, S., 2019. A new crustal model of the Anatolia-Aegean domain: evidence for the dominant role of isostasy in the support of the Anatolian plateau. Geophys. J. Int. 218, 57–73. https://doi.org/10.1093/gji/ggz147.

Karato, S., 1986. Does partial melting reduce the creep strength of the upper mantle? Nature 319, 309–310. https://doi.org/10.1038/319309a0.

Karato, S.i., Wu, P., 1993. Rheology of the upper mantle: a synthesis. Science 260, 771–778. https://doi.org/10.1126/science.260.5109.771.

Katz, R.F., Spiegelman, M., Langmuir, C.H., 2003. A new parameterization of hydrous mantle melting. Geochem. Geophys. Geosyst. 4 https://doi.org/10.1029/2002GC000433.
Kelemen, P.B., Hirth, G., Shimizu, N., Spiegelman, M., Dick, H.J., 1997. A review of melt migration processes in the adiabatically upwelling mantle beneath oceanic spreading ridges. Phil. Trans. R. Soc. A. 355, 283–318. https://doi.org/10.1098/rsta.1997.0010.
Kinzler, R.J., Grove, T.L., 1992. Primary magmas of mid-ocean ridge basalts 1. Experiments and methods. J. Geophys. Res.: Solid Earth 97, 6885–6906. https://doi.org/10.1029/91JB02840.
Klemme, S., 2004. The influence of cr on the garnet–spinel transition in the earth's mantle: experiments in the system mgo–cr2o3–sio2 and thermodynamic modelling. Lithos 77, 639–646. https://doi.org/10.1016/j.lithos.2004.03.017.
Klemme, S., Ivanic, T., Connolly, J., Harte, B., 2009. Thermodynamic modelling of cr-bearing garnets with implications for diamond inclusions and peridotite xenoliths. Lithos 112, 986–991. https://doi.org/10.1016/j.lithos.2009.05.007.
Kojitani, H., Akaogi, M., 1997. Melting enthalpies of mantle peridotite: calorimetric determinations in the system cao-mgo-al2o3-sio2 and application to magma generation. Earth Planet. Sci. Lett. 153, 209–222. https://doi.org/10.1016/S0012-821X(97)00186-6.
Kopylova, M.G., Caro, G., 2004. Mantle Xenoliths from the Southeastern Slave Craton: Evidence for Chemical Zonation in a Thick, Cold Lithosphere. J. Petrol. 45, 1045–1067. https://doi.org/10.1093/petrology/egh003.
Kreemer, C., Blewitt, G., Klein, E.C., 2014. A geodetic plate motion and global strain rate model. Geochem. Geophys. Geosyst. 15, 3849–3889. https://doi.org/10.1002/2014GC005407.
Kustowski, B., Ekström, G., Dziewoński, A.M., 2008. Anisotropic shear-wave velocity structure of the earth's mantle: A global model. Journal of Geophysical Research: Solid. Earth 113. https://doi.org/10.1029/2007JB005169.
Lachenbruch, A.H., Morgan, P., 1990. Continental extension, magmatism and elevation; formal relations and rules of thumb. Tectonophysics 174, 39–62. https://doi.org/10.1016/0040-1951(90)90383-J.
Lamb, S., Moore, J.D.P., Perez-Gussinye, M., Stern, T., 2020. Global whole lithosphere isostasy: implications for surface elevations, structure, strength, and densities of the continental lithosphere. Geochem. Geophys. Geosyst. 21, e2020GC009150 https://doi.org/10.1029/2020GC009150.
Langmuir, C.H., Forsyth, D.W., 2007. Mantle melting beneath mid-ocean ridges. Oceanography 1, 78–89.
Lavier, L., Buck, W.R., Poliakov, A.N.B., 2000. Factors controlling normal fault offset in an ideal brittle layer. J. Geophys. Res.: Solid Earth 105, 23431–23442. https://doi.org/10.1029/2000JB900108.
Lavier, L., Manatschal, G., 2006. A mechanism to thin the continental lithosphere at magma-poor margins. Nature 440, 324–328. https://doi.org/10.1038/nature04608.
Lavier, L., Roger Buck, W., Poliakov, A.N.B., 1999. Self-consistent rolling-hinge model for the evolution of large-offset low-angle normal faults. Geology 27, 1127–1130. https://doi.org/10.1130/0091-7613(1999)027<1127:SCRHMF>2.3.CO;2.
Lévy, F., Jaupart, C., 2011. Temperature and rheological properties of the mantle beneath the north american craton from an analysis of heat flux and seismic data. J. Geophys. Res.: Solid Earth 116. https://doi.org/10.1029/2010JB007726.
Li, C.F., Lu, Y., Wang, J., 2017. A global reference model of curie-point depths based on emag2. Sci. Rep. 7, 45129. https://doi.org/10.1038/srep45129.
Liu, C.Z., Dick, H.J., Mitchell, R.N., Wei, W., Zhang, Z.Y., Hofmann, A.W., Yang, J.F., Li, Y., 2022. Archean cratonic mantle recycled at a mid-ocean ridge. Sci. Adv. 8, eabn6749 https://doi.org/10.1126/sciadv.abn6749.
Liu, C.Z., Snow, J.E., Hellebrand, E., Brügmann, G., von der Handt, A., Büchl, A., Hofmann, A.W., 2008. Ancient, highly heterogeneous mantle beneath gakkel ridge, arctic ocean. Nature 452, 311–316. https://doi.org/10.1038/nature06688.
Louden, K., Osler, J., Srivastava, S., Keen, C., 1996. Formation of oceanic crust at slow spreading rates: New constraints from an extinct spreading center in the Labrador Sea. Geology 24, 771–774. https://doi.org/10.1130/0091-7613(1996)024<0771:FOOCAS>2.3.CO;2.
Lu, G., Huismans, R.S., 2021. Melt volume at atlantic volcanic rifted margins controlled by depth-dependent extension and mantle temperature. Nature. Communications 12, 3894. https://doi.org/10.1038/s41467-021-23981-5.
Mackwell, S.J., Zimmerman, M.E., Kohlstedt, D.L., 1998. High-temperature deformation of dry diabase with application to tectonics on venus. J. Geophys. Res.: Solid Earth 103, 975–984. https://doi.org/10.1029/97JB02671.
Martinez, F., Hey, R., Höskuldsson, Á., 2020. Reykjanes ridge evolution: effects of plate kinematics, small-scale upper mantle convection and a regional mantle gradient. Earth-Sci. Rev. 206, 102956. https://doi.org/10.1016/j.earscirev.2019.102956.
Matthews, S., Wong, K., Shorttle, O., Edmonds, M., Maclennan, J., 2021. Do olivine crystallization temperatures faithfully record mantle temperature variability? Geochem. Geophys. Geosyst. 22, e2020GC009157 https://doi.org/10.1029/2020GC009157.
McDonough, W., Sun, s.S., 1995. The composition of the earth. Chem. Geol. 120, 223–253. https://doi.org/10.1016/0009-2541(94)00140-4.
McKenzie, D., 1978. Some remarks on the development of sedimentary basins. Earth Planet. Sci. Lett. 40, 25–32. https://doi.org/10.1016/0012-821X(78)90071-7.
McKenzie, D., Bickle, M.J., 1988. The Volume and Composition of Melt Generated by Extension of the Lithosphere. J. Petrol. 29, 625–679. https://doi.org/10.1093/petrology/29.3.625.
Meibom, A., Anderson, D.L., 2004. The statistical upper mantle assemblage. Earth Planet. Sci. Lett. 217, 123–139. https://doi.org/10.1016/S0012-821X(03)00573-9.
Molnar, P., England, P., 1990. Late cenozoic uplift of mountain ranges and global climate change: chicken or egg? Nature 346, 29–34. https://doi.org/10.1038/346029a0.
Molnar, P., England, P.C., Jones, C.H., 2015. Mantle dynamics, isostasy, and the support of high terrain. J. Geophys. Res.-Solid Earth 120, 1932–1957. https://doi.org/10.1002/2014JB011724.
Morgan, W.J., Morgan, J.P., 2007. Plate velocities in the hotspot reference frame. In: Plates, Plumes and Planetary Processes. Geological Society of America. https://doi.org/10.1130/2007.2430(04).
Munch, F.D., Khan, A., Tauzin, B., van Driel, M., Giardini, D., 2020. Seismological evidence for thermo-chemical heterogeneity in earth's continental mantle. Earth Planet. Sci. Lett. 539, 116240. https://doi.org/10.1016/j.epsl.2020.116240.
Müller, R.D., Sdrolias, M., Gaina, C., Roest, W.R., 2008. Age, spreading rates, and spreading asymmetry of the world's ocean crust. Geochem. Geophys. Geosyst. 9 https://doi.org/10.1029/2007GC001743.
Nielsen, T.K., Hopper, J.R., 2004. From rift to drift: Mantle melting during continental breakup. Geochem. Geophys. Geosyst. 5 https://doi.org/10.1029/2003GC000662.
Niu, Y., 2017. The Meaning of Global Ocean Ridge Basalt Major Element Compositions. J. Petrol. 57, 2081–2103. https://doi.org/10.1093/petrology/egw073.
Niu, Y., 2021. Lithosphere thickness controls the extent of mantle melting, depth of melt extraction and basalt compositions in all tectonic settings on earth – a review and new perspectives. Earth-Sci. Rev. 217, 103614. https://doi.org/10.1016/j.earscirev.2021.103614.
Niu, Y., Batiza, R., 1991. An empirical method for calculating melt compositions produced beneath mid-ocean ridges: application for axis and off-axis (seamounts) melting. J. Geophys. Res.: Solid Earth 96, 21753–21777. https://doi.org/10.1029/91JB01933.
O'Reilly, S., Griffin, W., 2006. Imaging global chemical and thermal heterogeneity in the subcontinental lithospheric mantle with garnets and xenoliths: geophysical implications. Tectonophysics 416, 289–309. https://doi.org/10.1016/j.tecto.2005.11.014.
Oxburgh, E.R., Parmentier, E.M., 1977. Compositional and density stratification in oceanic lithosphere-causes and consequences. Journal of the Geological Society 133, 343–355. https://doi.org/10.1144/gsjgs.133.4.0343.
Poupinet, G., Shapiro, N., 2009. Worldwide distribution of ages of the continental lithosphere derived from a global seismic tomographic model. Lithos 109, 125–130. https://doi.org/10.1016/j.lithos.2008.10.023.
Pratt, J.H., 1859. On the deflection of the plumb-line in india, caused by the attraction of the himmalaya mountains and of the elevated regions beyond; and its modification by the compensating effect of a deficiency of matter below the mountain mass. Philos. Trans. R. Soc. Lond. 149, 745–778. https://doi.org/10.1098/rspl.1857.0096.
Presnall, D.C., Gudfinnsson, G.H., Walter, M.J., 2002. Generation of mid-ocean ridge basalts at pressures from 1 to 7 gpa. Geochim. Cosmochim. Acta 66, 2073–2090. https://doi.org/10.1016/S0016-7037(02)00890-6.
Reguzzoni, M., Sampietro, D., 2015. Gemma: an earth crustal model based on goce satellite data. Int. J. Appl. Earth Observ. Geoinf. 35, 31–43. https://doi.org/10.1016/j.jag.2014.04.002.
Reston, T.J., Morgan, J.P., 2004. Continental geotherm and the evolution of rifted margins. Geology 32, 133–136. https://doi.org/10.1130/G19999.1.
Ribe, N., Christensen, U., Theißing, J., 1995. The dynamics of plume-ridge interaction, 1: ridge-centered plumes. Earth Planet. Sci. Lett. 134, 155–168. https://doi.org/10.1016/0012-821X(95)00116-T.
Richards, F.D., Hoggard, M.J., Cowton, L.R., White, N.J., 2018. Reassessing the thermal structure of oceanic lithosphere with revised global inventories of basement depths and heat flow measurements. J. Geophys. Res.: Solid Earth 123, 9136–9161. https://doi.org/10.1029/2018JB015998.
Roberts, A., Kusznir, N., Yielding, G., Styles, P., 1998. 2d flexural backstripping of extensional basins; the need for a sideways glance. Petrol. Geosci. 4, 327–338.
Röhm, A.H., Snieder, R., Goes, S., Trampert, J., 2000. Thermal structure of continental upper mantle inferred from s-wave velocity and surface heat flow. Earth Planet. Sci. Lett. 181, 395–407. https://doi.org/10.1016/S0012-821X(00)00209-0.
Rowley, D.B., 2018. Oceanic axial depth and age-depth distribution of oceanic lithosphere: Comparison of magnetic anomaly picks versus age-grid models. Lithosphere 11, 21–43. https://doi.org/10.1130/L1027.1.
Ryan, W.B.F., Carbotte, S.M., Coplan, J.O., O'Hara, S., Melkonian, A., Arko, R., Weissel, R.A., Ferrini, V., Goodwillie, A., Nitsche, F., Bonczkowski, J., Zemsky, R., 2009. Global multi-resolution topography synthesis. Geochem. Geophys. Geosyst. 10 https://doi.org/10.1029/2008GC002332.
Schaeffer, A.J., Lebedev, S., 2013. Global shear speed structure of the upper mantle and transition zone. Geophys. J. Int. 194, 417–449. https://doi.org/10.1093/gji/ggt095.
Schutt, D.L., Lesher, C.E., 2006. Effects of melt depletion on the density and seismic velocity of garnet and spinel lherzolite. J. Geophys. Res.: Solid Earth 111. https://doi.org/10.1029/2003JB002950.
Scott, D.R., 1992. Small-scale convection and mantle melting beneath mid-ocean ridges. Washington DC Am. Geophys. Union Geophys. Monogr. Ser. 71, 327–352. https://doi.org/10.1029/GM071p0327.
Scott, D.R., Stevenson, D.J., 1989. A self-consistent model of melting, magma migration and buoyancy-driven circulation beneath mid-ocean ridges. J. Geophys. Res.: Solid Earth 94, 2973–2988. https://doi.org/10.1029/JB094iB03p02973.
Simon, K., Huismans, R.S., Beaumont, C., 2009. Dynamical modelling of lithospheric extension and small-scale convection: implications for magmatism during the formation of volcanic rifted margins. Geophys. J. Int. 176, 327–350. https://doi.org/10.1111/j.1365-246X.2008.03891.x.
Simon, N.S., Podladchikov, Y.Y., 2008. The effect of mantle composition on density in the extending lithosphere. Earth Planet. Sci. Lett. 272, 148–157. https://doi.org/10.1016/j.epsl.2008.04.027.
Spiegelman, M., 1993. Physics of melt extraction: theory, implications and applications. Philos. Trans. Royal Soc. London Ser. A: Phys. Eng. Sci. 342, 23–41. https://doi.org/10.1098/rsta.1993.0002.

Steinberger, B., Becker, T.W., 2018. A comparison of lithospheric thickness models. Tectonophysics 746, 325–338. https://doi.org/10.1016/j.tecto.2016.08.001. URL: http://www.sciencedirect.com/science/article/pii/S004019511630316X. understanding geological processes through modelling - A Memorial Volume honouring Evgenii Burov.

Sternai, P., 2020. Surface processes forcing on extensional rock melting. Sci. Rep. 10, 7711. https://doi.org/10.1038/s41598-020-63920-w.

Stixrude, L., Lithgow-Bertelloni, C., 2011. Thermodynamics of mantle minerals - II. Phase equilibria. Geophys. J. Int. 184, 1180–1213. https://doi.org/10.1111/j.1365-246X.2010.04890.x.

Stixrude, L., Lithgow-Bertelloni, C., 2012. Geophysics of chemical heterogeneity in the mantle. Annu. Rev. Earth Planet. Sci. 40, 569–595. https://doi.org/10.1146/annurev.earth.36.031207.124244.

Straume, E.O., Gaina, C., Medvedev, S., Hochmuth, K., Gohl, K., Whittaker, J.M., Abdul Fattah, R., Doornenbal, J.C., Hopper, J.R., 2019. Globsed: updated total sediment thickness in the world's oceans. Geochem. Geophys. Geosyst. 20, 1756–1772. https://doi.org/10.1029/2018GC008115.

Svartman Dias, A.E., Lavier, L., Hayman, N.W., 2015. Conjugate rifted margins width and asymmetry: The interplay between lithospheric strength and thermomechanical processes. J. Geophys. Res.: Solid Earth 120, 8672–8700. https://doi.org/10.1002/2015JB012074.

Takahashi, E., Shimazaki, T., Tsuzaki, Y., Yoshida, H., 1993. Melting study of a peridotite klb-1 to 6.5 gpa, and the origin of basaltic magmas. Philos. Trans.: Phys. Sci. Eng. 342, 105–120. https://doi.org/10.1098/rsta.1993.0008.

Team, T.M.S., 1998. Imaging the deep seismic structure beneath a mid-ocean ridge: The melt experiment. Science 280, 1215–1218. https://doi.org/10.1126/science.280.5367.1215.

Tenzer, R., Chen, W., 2019. Mantle and sub-lithosphere mantle gravity maps from the litho1.0 global lithospheric model. Earth-Sci. Rev. 194, 38–56. https://doi.org/10.1016/j.earscirev.2019.05.001.

Tenzer, R., Chen, W., Tsoulis, D., Bagherbandi, M., Sjöberg, L.E., Novák, P., Jin, S., 2015. Analysis of the refined crust1.0 crustal model and its gravity field. Surv. Geophys. 36, 139–165. https://doi.org/10.1007/s10712-014-9299-6.

Theunissen, T., Huismans, R.S., 2019. Long-term coupling and feedback between tectonics and surface processes during non-volcanic rifted margin formation. J. Geophys. Res.: Solid Earth 124, 12323–12347. https://doi.org/10.1029/2018JB017235.

Theunissen, T., Huismans, R.S., 2022. Mantle exhumation at magma-poor rifted margins controlled by frictional shear zones. Nature. Communications 13, 1634. https://doi.org/10.1038/s41467-022-29058-1.

Thieulot, C., 2011. Fantom: Two- and three-dimensional numerical modelling of creeping flows for the solution of geological problems. Phys. Earth Planet. Inter. 188, 47–68. https://doi.org/10.1016/j.pepi.2011.06.011.

Torsvik, T.H., Amundsen, H.E.F., Trønnes, R.G., Doubrovine, P.V., Gaina, C., Kusznir, N. J., Steinberger, B., Corfu, F., Ashwal, L.D., Griffin, W.L., Werner, S.C., Jamtveit, B., 2015. Continental crust beneath southeast iceland. Proc. Natl. Acad. Sci. 112, E1818–E1827. https://doi.org/10.1073/pnas.1423099112.

Turcotte, D.L., Schubert, G., 1982. Geodynamics applications of continuum physics to geological problems. John Wiley and Sons, Inc., United States, New York, NY (US).

Vinnik, L.P., Foulger, G.R., Du, Z., 2005. Seismic boundaries in the mantle beneath Iceland: a new constraint on temperature. Geophys. J. Int. 160, 533–538. https://doi.org/10.1111/j.1365-246X.2005.02529.x.

Watts, A., 2001. Isostasy and flexure of the lithosphere. Cambridge University Press. ISBN: 9780521006002.

Watts, A., Ryan, W., 1976. Flexure of the lithosphere and continental margin basins. Tectonophysics 36, 25–44. https://doi.org/10.1016/0040-1951(76)90004-4.

Watts, A.B., 2021. Isostasy. Springer International Publishing, Cham, pp. 831–847. https://doi.org/10.1007/978-3-030-58631-7_81.

Watts, A.B., Moore, J.D.P., 2017. Flexural isostasy: constraints from gravity and topography power spectra. J. Geophys. Res.: Solid Earth 122, 8417–8430. https://doi.org/10.1002/2017JB014571.

White, R.S., Minshull, T.A., Bickle, M.J., Robinson, C.J., 2001. Melt generation at very slow-spreading oceanic ridges: constraints from geochemical and geophysical data. J. Petrol. 42, 1171–1196. https://doi.org/10.1093/petrology/42.6.1171.

Wojciechowski, M., 2018. A note on the differences between drucker-prager and mohr-coulomb shear strength criteria. Stud. Geotech. Mech. 40, 163–169. https://doi.org/10.2478/sgem-2018-0016.

Wolf, S.G., Huismans, R.S., Braun, J., Yuan, X., 2022. Topography of mountain belts controlled by rheology and surface processes. Nature 606, 516–521. https://doi.org/10.1038/s41586-022-04700-6.

Yan, J., Ballmer, M.D., Tackley, P.J., 2020. The evolution and distribution of recycled oceanic crust in the earth's mantle: insight from geodynamic models. Earth Planet. Sci. Lett. 537, 116171. https://doi.org/10.1016/j.epsl.2020.116171.

Zha, C., Lin, J., Zhou, Z., Xu, M., Zhang, X., 2022. Effects of hotspot-induced long-wavelength mantle melting variations on magmatic segmentation at the reykjanes ridge: insights from 3d geodynamic modeling. J. Geophys. Res.: Solid Earth 127, e2021JB023244. https://doi.org/10.1029/2021JB023244.

Ziberna, L., Klemme, S., 2016. Application of thermodynamic modelling to natural mantle xenoliths: examples of density variations and pressure–temperature evolution of the lithospheric mantle. Contrib. Miner. Petrol. 171, 16. https://doi.org/10.1007/s00410-016-1229-9.

Zindler, A., Hart, S., 1986. Chemical geodynamics. Annu. Rev. Earth Planet. Sci. 14, 493–571. https://doi.org/10.1146/annurev.ea.14.050186.002425.

Zoback, M.L., Mooney, W.D., 2003. Lithospheric buoyancy and continental intraplate stresses. Int. Geol. Rev. 45, 95–118. https://doi.org/10.2747/0020-6814.45.2.95.